Individual cell-based models of cell scatter of aro and mlp-29 cells in response to hepatocyte growth factor

Marco Scianna, Roeland M.H. Merks, Luigi Preziosi, Enzo Medico

www.elsevier.com/locate/yjtbi

Individual cell-based models of cell scatter of aro and mlp-29 cells in response to hepatocyte growth factor

Marco Scianna, Roeland M.H. Merks, Luigi Preziosi, Enzo Medico

PII: S0022-5193(09)00233-1
DOI: doi:10.1016/j.jtbi.2009.05.017
Reference: YJTBI 5563

To appear in: *Journal of Theoretical Biology*

Received date: 22 November 2008
Revised date: 13 May 2009
Accepted date: 13 May 2009

Cite this article as: Marco Scianna, Roeland M.H. Merks, Luigi Preziosi and Enzo Medico, Individual cell-based models of cell scatter of aro and mlp-29 cells in response to hepatocyte growth factor, *Journal of Theoretical Biology*, doi:10.1016/j.jtbi.2009.05.017

INDIVIDUAL CELL-BASED MODELS OF CELL SCATTER OF ARO AND MLP-29 CELLS IN RESPONSE TO HEPATOCYTE GROWTH FACTOR

MARCO SCIANNA[1,4], **ROELAND M. H. MERKS**[2,3], **LUIGI PREZIOSI**[1,*] **and ENZO MEDICO**[4]

[1] *Department of Mathematics, Politecnico di Torino, Corso Duca degli Abruzzi 24, 10129 Torino, Italy*

[2] *NCSB-NISB, Kruislaan 318, Amsterdam, Netherlands*

[3] *CWI, Science Park 123, 1098 XG Amsterdam, Netherlands*

[4] *Department of Oncological Sciences and Laboratory of Oncogenomics, Institute for Cancer Research and Treatment, University of Torino, S.P. 142, 10060 Candiolo (Torino), Italy*

[*]**Corresponding authors**: luigi.preziosi@polito.it

Abstract

The different behaviors of colonies of two cell lines, ARO (tyroid carcinoma-derived cells) and MLP-29 (Mouse Liver Progenitor cells), in response to Hepatocyte Growth Factor (HGF) are described deducing suitable Cellular Potts Models (CPM). It is shown how increased motility and decreased adhesiveness are responsible for cell-cell dissociation and tissue invasion in the ARO cells. On the other hand, it is shown that, in addition to the biological mechanisms above, it is necessary to include directional persistence in cell motility and HGF diffusion to describe the scattering and the branching processes characteristic of MLP-29 cells.

Keywords: Cellular Potts Model, Hepatocyte Growth Factor, ARO cell line, cell-cell dissociation, invasive growth, MLP-29 cell line, scattering.

Introduction and Phenomenological Description

Hepatocyte Growth Factor (HGF), originally identified as a mitogen for hepatocytes [23, 24], was subsequently shown to be identical to Scatter Factor (SF) [1, 6, 7], a ligand with a dramatically different activity of inducing epithelial cells dissociation [5]. HGF, produced primarily by mesenchymal cells, is therefore a unique growth factor that elicits multiple cellular responses, via its receptor, a tyrosine kinase encoded by the proto-oncogene Met [17, 18].

The main biological processes regulated by HGF are mitogenesis, motility and morphogenesis [29, 31], cell dissociation, migration through the extracellular matrix, acquisition of polarity and tubule formation [26, 28]. This combination of events, also known as "invasive growth", is fundamental during the embryonic development of most epithelial tissues. When inappropriately activated, this genetic program confers invasive ability to normal and neoplastic epithelial cells [23, 32].

Increased levels of the HGF receptor Met have been observed in primary thyroid cells [14, 21], suggesting that Met may mediate some of the phenotypic alterations observed in these cells: these data allowed to precisely define the role

of the HGF and its receptor in the evolution of thyroid tumors, finding which of the many cellular events, known to follow Met activation, effectively take place in thyroid cancer cells.

In this work we analyze the biological responses to HGF of a poorly differentiated thyroid carcinoma-derived cell line, ARO, that overexpresses Met [9]. In these cells, HGF stimulation doesn't make the growth rate increase, probably due to the high basal level of proliferation, but it increases motility [8].

In particular, HGF induces a mesenchymal transition with a dramatic change from a virtually non motile phenotype to a phenotype with high short range motility: cells loosen contacts, dissociate, move from their original site and start wondering in the close proximity, displaying an evident ability to invade the open spaces and modifying the interaction with the extracellular matrix (see Fig. 1 and Supp. Movie 1). Noteworthy, in response to HGF, ARO cells do not show a dramatic cytoskeletal reorganization or polarization but lose their tendency to maximize the contact area with the surrounding cells and the physiological regulation of contact-inhibition mechanism. The change in the above mentioned adhesive properties is a consequence of the change in the transmission of a number of local, contact-dependent signals (juxtracrine). In fact, we can hypothesize that the loss of intercellular adhesions does not cause by itself a dissociation phenotype, since E-cadherin -/- cells may still form strong adhesive junctions. Instead the loss of E-cadherin signaling may be responsible for this behavior [20, 25]. The above assumptions are validated also by the fact that in absence of HGF the transmission of the juxtracrine is recovered so that the dissociated, disconnected cells have the tendency to come again in contact and to form new compact colonies (not shown).

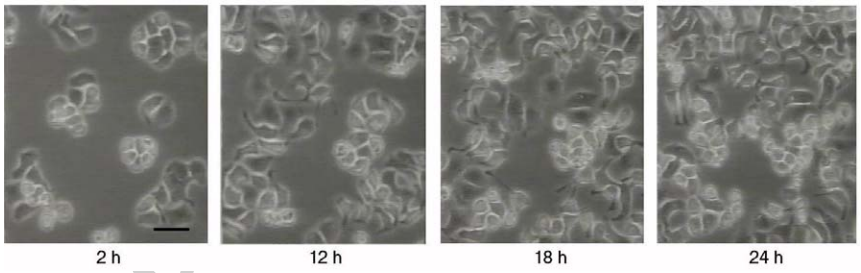

Figure 1: Phase contrast time-lapse microscopy of in vitro dissociation and migration of ARO cells, grown in 10 per cent fetal calf serum and incubated in the presence of 100 U/ml of hepatocyte growth factor for 2 h, 12 h, 18 h and 24 h. Scale bar, 25 μm long. The full time-lapse movie is provided in supplemental material and available in `calvino.polito.it/~preziosi/AROex.avi`.

Another scattering example is given by cultures of MLP-29, a strongly HGF-responsive epithelial cell line established from mouse embryonic liver. MLP-29 are small cells with ovoidal nuclei, forming tightly packed colonies.

After the addition of nanomolar concentration of HGF, the cells start to elongate, migrate and differentiate and the islands assume the characteristic stellar configuration within 1 day (as shown in Fig. 2 and Supp. Movie 2, also at at `calvino.polito.it/~preziosi/MLPex.avi`). This morphogenic response is dose dependent and consists of three steps:

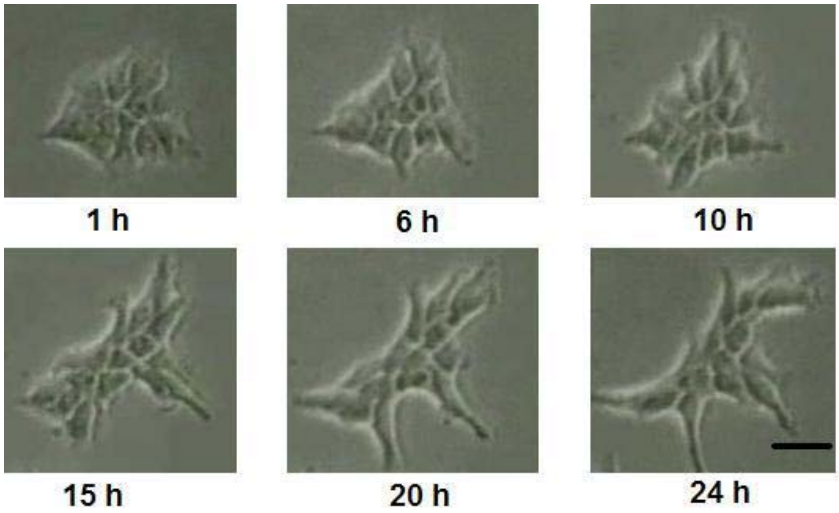

Figure 2: Typical time sequence of in vitro branching morphogenesis of a colony of MLP-29 cells, incubated for 24 h in DMEM - 1 % FCS, containing recombinant HGF, diluted to the final concentration of 100 ng/ml, at 1 h, 6 h, 10 h, 15 h, 20 h and 24 h after incubation. Scale bar is 25 μm long. The full time-lapse movie is provided in supplemental material and available in `calvino.polito.it/~preziosi/MLPex.avi`

1. within the first 6 h, the colony borders start roughening and most of cellular junctions (but not all) start breaking or reorganizing;

2. in the following 6 h there is a cytoskeletal reorganization, followed by an asymmetric polarization and an active migration of cells, which lead to the formation of some sprouts;

3. within 24 hours, at the end of the branching process, the colonies assume the stellar shape, with sprouts formed by one or few elongated cells that keep a thin adhesion contact with the rest of the island.

None of these events is observed in control medium or after stimulation with other growth factors: in those cases, MLP-29 cells tend to form spherical and compact aggregates of undifferentiated, almost round cells, with the interstitial spaces almost filled with microvilli protruding from the cell surface along the entire perimeter of each cell [23].

Entering more in details in the description of HGF-driven scattering, the cells in the middle of an island don't have a dramatic change of shape, keeping their original elliptical shape, and passively move only dragged by the nearest sprout.

Instead, the cells at the margin acquire a polar configuration driven by an internal remodeling of the actin cytoskeleton: they are highly asymmetric and have distinct apical, lateral and basal surfaces which correspond to a leading and trailing surface during their migration. In particular, they migrate faster along their long axes than along their short axes, because they need fewer surface protrusions and retractions to move normal to their short interface than to their long interface. Such anisotropic, cell-shape-dependent motility results in strong

directional persistence because the cells must reorient before moving into a new direction. This inertial dynamic introduces two timescales into scattering: fast migration along the cells' long axes produces rapid branching and polarization, the slower sideways migration coarsens the pattern as the cells align and close small lacunae.

The polarized cells, in the part of their surface in contact with the ECM, extend filopodia towards the open space and keep a thin adhesion point with the main corpus of the colony. The branches, generally formed by couples of parallel elongated cells, are radially disposed with angles ranging between 15 and 100 degrees. If the HGF is no longer added in the culture a sort of involution of the sprouts is seen and the colonies tend to become round and compact again (not shown).

We here model the just described behavior of both ARO and MLP-29 cell lines at a mesoscopic level using the Cellular Potts Model (a lattice-based, Monte Carlo approach developed for instance in [13, 19, 20, 21, 22]), which allows to describe cell-cell adhesion and cell migration. An energy minimization philosophy, a set of constraints and auxiliary conditions determine how the cells move. In particular intercellular junctions determine an adhesive (or binding) energy between cells and an energy constraint regulates cell volume.

We show also how, with respect to ARO colonies, in order to describe the behavior of MLP-29 colonies it is necessary to include in the model a specific term mimicking cell persistence. In both cases, we assume that the HGF is not limiting and distributes uniformly over the ECM.

The results of the simulations are in good agreement with the experiments obtaining all the described features and morphologies characterizing the evolution of both cell lines .

Cellular Potts Model

We use the CPM and make all of our biological assumptions at the cell level, while discussing the model results at the level of the tissue. Our basic model is referred to the case of the ARO cells and assumes that (a) the cells keep a round shape, (b) the addition of the growth factor influences the cell-cell adhesion energy and the system motility, leading to the dissociation and invasion processes and (c) the E-cadherin binding at cell-cell interfaces represses the formation of surface projections (filopodia), while they form normally at the unbound parts of the cell surface in contact with the extracellular matrix (contact-inhibition).

The CPM represents biological cells as patches of lattice spins $\sigma(\mathbf{x})$ of identical state on a second-nearest-neighbor square lattice, where each state labels a single biological cells, see Fig. 3A. Connections between neighboring lattice sites of unlike state $\sigma(\mathbf{x}) \neq \sigma(\mathbf{x}')$ represent membrane bonds between cells, where the non-dimensional parameters $J_{\sigma(\mathbf{x}),\sigma(\mathbf{x}')}$ give the bond energy, assuming that the types and the number of E-cadherins and other adhesive cell-surface proteins determine the Js. Since in our model there is only a type of cells placed in a virtual extracellular matrix the Js reduce to $J_{c,M}$ and $J_{c,c}$, where c represents a cell and M the ECM, Fig. 3B. We further define the relative adhesion through the parameter $\gamma_{c,M} = J_{c,M} - J_{c,c}/2$, which enables us to determine whether the cells cohere ($\gamma_{c,M} < 0$) or dissociate ($\gamma_{c,M} > 0$).

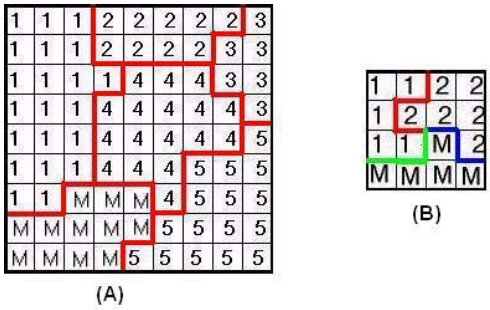

Figure 3: (A) Typical square grid of the CPM. The single cells are labeled by the same spin. (B) Membrane bonds between different cells (color lines). In each picture the ECM is represented by the lattice sites of index M.

An energy penalty increasing with the cells' deviation from a designed target volume, A_σ, constraints the volume of the cells a_σ, i.e. A_σ and a_σ are expressed in lattice sites. We express the adhesion and target area deviations in terms of the effective energy H:

$$H = \sum_{\mathbf{x},\mathbf{x}'} J_{\sigma(\mathbf{x}),\sigma(\mathbf{x}')}(1 - \delta_{\sigma(\mathbf{x}),\sigma(\mathbf{x}')}) + \lambda \sum_{\sigma} (a_\sigma - A_\sigma)^2, \tag{1}$$

where $\mathbf{x}'$ represents the eight second-order neighbors of $\mathbf{x}$, the non-dimensional Lagrangian multiplier λ the cells' resistance to compression and the Kroenecker delta is $\delta_{x,y} = \{1, x = y; 0, x \neq y\}$. The cells reside in an ECM which we model as generalized CPM cells without a volume constraint and with $\sigma = 0$. We define a special, high cell-border energy $J_{c,B} = 100$ to prevent cells from adhering to the boundaries of the simulated area (which we define as frozen pixels of type B).

To mimic cytoskeletally driven, active surface fluctuations, we randomly choose a lattice site, $\mathbf{x}$, and attempt to copy its spin $\sigma(\mathbf{x})$ into a randomly chosen neighboring lattice site $\mathbf{x}'$. For better isotropy we use the twenty, first to four nearest neighbors. This attempt represents a lamellipodial or filopodial protrusion of the first cell displacing the surface of the second cell. During a Monte Carlo Step (MCS), which can be evaluated to be 30 seconds long from a direct comparison of simulations and experiments, we attempt a number of copies equal to the number of sites in the lattice. We minimize H using standard Metropolis dynamics: we calculate how much the free energy H would change if we performed the copy and accept the attempt with Boltzmann probability:

$$P(\Delta H) = \begin{cases} e^{\frac{-\Delta H - H_0}{T}} & \Delta H \geq -H_0 \\ 1 & \Delta H < -H_0 \end{cases} \tag{2}$$

where H_0 is an energy threshold which models viscous dissipation and energy loss during bond breakage and formation and the non-dimensional coefficient T is related to cell motility. Each CPM cell i moves according to the effective-energy gradient around it, $\mathbf{v}_i \propto \nabla_i H$, where $\nabla_i H$ is the component of the gradient relative to cell i. Thus, given an effective energy, we can calculate the resulting cell motion and the force required to create such a motion. In the

highly viscous environment of the ECM, the drag force $\mathbf{F}_i$ exerted on a cell i is proportional to its velocity $\mathbf{v}_i$: this relation is often called the overdamped force-velocity response. Thus the force exerted on a cell is proportional to the effective energy gradient $\mathbf{F}_i \propto \nabla_i H$.

In the case of ARO aggregates, HGF stimulation is modeled only through its effects on cell-cell adhesion energy and on cellular motility. In fact we can preliminary hypothesize a directed proportionality between the virtual HGF concentration and both the model parameters T and $J_{c,c}$, so that increasing doses of the growth factor correspond to increasing values of cellular motility T and of inter-cellular adhesion coefficient $J_{c,c}$, mimicking weaker cell-cell junctions. $J_{c,M}$ remains fixed in each simulation, since in this model the matrix is only considered as a rigid thin layer formed by generalized cells, that are not represented in the CPM lattice and not influenced by HGF.

As we shall see, the basic model (1) is not able to predict the behavior of the MLP-29 cells. In fact, in a culture of MLP-29 cells, the growth factor induces also cell elongation and polarization. These ingredients, that are not contained in (1), are essential for branching morphogenesis and the formation of the stellar shape aggregates experimentally found.

In fact, still trying to keep contact with the colony, MLP-29 cells take time to reorganize their internal machinery to change their direction of motion and their orientation and polarization induce a persistence motion, as done in [12]. We can model this cytoskeletal persistence time by adding to our effective energy H an *inertial-like term* of the form:

$$H_{in} = \lambda_{in} \sum_{\mathbf{x},\mathbf{x}'} ||\mathbf{v}(\sigma,t) - \mathbf{v}(\sigma,t-\Delta t)||^2 \tag{3}$$

where $\mathbf{v}(\sigma,t)$

$$\mathbf{v}(\sigma,t) = \frac{\mathbf{cm}(\sigma,t) - \mathbf{cm}(\sigma,t-\Delta t)}{\Delta t}, \tag{4}$$

is the instantaneous center of mass ($\mathbf{cm}(\sigma) = a^{-1}(\sigma)\sum_{\mathbf{x}:\sigma(\mathbf{x})=\sigma}\mathbf{x}$) velocity of cell σ and the non-dimensional Lagrangian multiplier λ_{in} controls the persistence time. Typically, Δt is one or more MCS. Obviously, if $\lambda_{in} = 0$ cells undergo uncorrelated Brownian motion, while if λ_{in} is large the motion is almost ballistic.

In this case, it is also needed to add a PDE to model the diffusion and absorption of HGF in the culture from a macroscopical point of view [21, 22]: the equation regulating the evolution in time of the growth factor is

$$\frac{\partial h}{\partial t} = \alpha - \varepsilon\delta_{\sigma(\mathbf{x}),0}h + D\nabla^2 h \tag{5}$$

where

$$\delta_{\sigma(\mathbf{x}),0} = \begin{cases} 1 & \text{inside the cell} \\ \\ 0 & \text{in the ECM,} \end{cases} \tag{6}$$

α is the rate at which the HGF is uniformly added, ε is the uptake rate of the growth factor and D the diffusion constant, which will be always set to $10^{-13}\mathrm{m}^2\mathrm{s}^{-1}$, as done in [20]. In every experiment, the secretion and the decay

rate are set equal, see also [21]: for our parameter settings the HGF diffuses more rapidly than the cells move, enabling us to ignore advection which may occur as the cells displace the ECM.

We implement chemotaxis due to preferential extension of pseudopods up HGF gradients by including a chemical energy change at each copy [19, 20, 21]:

$$\Delta H_{chemotaxis} = -\mu \left(h(\mathbf{x}') - h(\mathbf{x}) \right), \tag{7}$$

where h is the concentration of HGF, which, as said, we assume is present everywhere in the layer of HGF under the cells, $\mathbf{x}'$ is the target site and $\mathbf{x}$ the source site. In this case chemotaxis depends on the HGF gradient only, independently of its concentration.

The chemotaxis coefficient μ is set equal to 0 at cell-cell interfaces and to 500 at cell-ECM interfaces, ensuring that chemotactic extensions occur only at cell-ECM surfaces, mimicking contact-inhibition chemotaxis.

The PDE is solved numerically using a finite difference scheme on a lattice that matches the CPM lattice, using 15 diffusion steps per MCS, i.e. the time step for the diffusion solver is 2 sec and the space step is 2 μm.

To sum up, the scheme used for MLP-29 cell line consists of an hybrid CPM/PDE model: the CPM models the cells, the PDE models the diffusion and the absorption of the growth factor.

Also in the MLP case, each Monte Carlo Step (MCS) corresponds to 30 s: for this choice of timescale, the mean of the cell velocities agrees well with in vivo observations.

Simulation of the Scattering Process of ARO Cells

Figure 4A-D shows a typical simulation of the time-sequence evolution of a culture of ARO cells in presence of HGF: we initiate the simulation with a mass of 16 virtual cells over an area of 300×300 lattice sites, which we positioned in a larger lattice of 500×500 to minimize boundary effects. Each CPM lattice site corresponds to a square of size 2 μm $\times$ 2 μm. We assume that cells do not divide or grow during patterning and set the target area of the simulated ARO cells to 50 lattice site, corresponding to 200 μm^2.

Based on cell culture measurements [8, 20], we set $\lambda = 25$, $J_{c,c} = 60$, $J_{c,M} = 20$ and T=50. After an initial roughening, the cells start to detach and to radially spread in close proximity, keeping an almost elliptical shape. In Fig. 4E-H we also simulate the loss of HGF in the culture medium by decreasing $J_{c,c}$ to 20, maintaining the other parameters fixed: as in the experiments, the cells aggregate again in an almost round compact island, confirming the hypothesis of the recovered E-cadherin signalling.

The evolution of the simulated colony coincides well with the experimental evidences, having also the same temporal dynamics, as shown in Fig. 5, where we plot the Scattering Index

$$S_I(t) = \frac{A(t)}{A(0)} - 1, \tag{8}$$

with $A(t)$ defined as the area of the minimal convex polygon with vertices at the more external cells (at the tips of the branches in MLP29 case) at time t and $A(0)$ at $t = 0$.

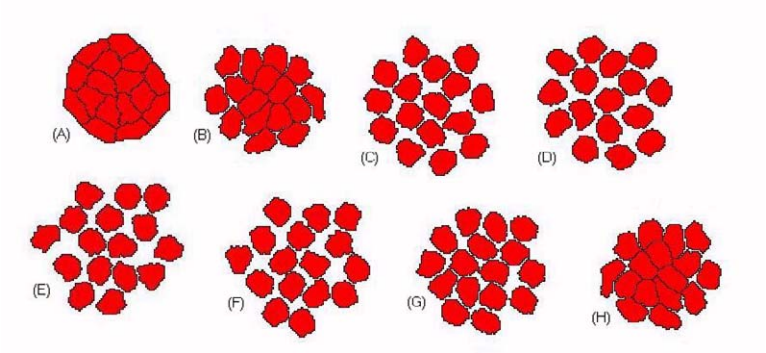

Figure 4: Cell-cell dissociation process in a simulation initiated with a clump of 16 ARO cells: (A) 6 hours, (B) 12 hours, (C) 18 hours, (D) 24 hours, (E) 30 hours, (F) 36 hours, (G) 42 hours and (H) 48 hours. After 3000 MCS ($\approx$ 24 hours) the HGF is no longer added in the culture. Full simulation is available at `calvino.polito.it/~preziosi/AROsim.avi`.

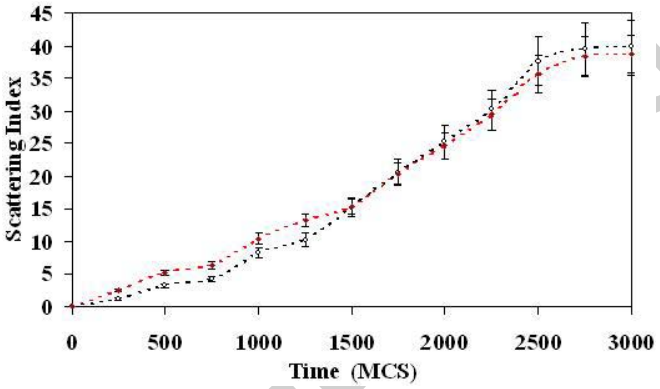

Figure 5: Comparison of the evolution in time of the Scattering Index of ARO cells for experimental (black dotted line) and simulation (red dotted line) evidences. Error bars show standard deviations over ten representative colonies for the experiments and over ten simulations.

The experimental scatter begins slightly slower than the simulated, however, after the initial phase ($t > 1500$ MCS), S_I increases at comparable rates in both cases.

To further study the robustness of the model and to identify the critical features of the output components, we analyze how the results of the simulations depend on the parameters by measuring the Scattering Index after 3000 MCS (i.e., 1 day). Fig. 6 shows that, at suitable T, our simulated aggregates do not scatter for low values of inter-cellular adhesion parameter $J_{c,c}$, corresponding to strong inter-cellular adhesion, whereas they dissociates when cells adhere less strongly: this observation corresponds well with our experiments where ARO aggregates scatter at high concentration of HGF, see [8]. In Fig. 6 we also look for the motilities required for the process: for $T < 30$ there is no detectable scattering within the time limit (3000 MCS), independently from the adhesion energies $J(c, c)$ (the cells dissociate, but don't spread away), for $T > 60$

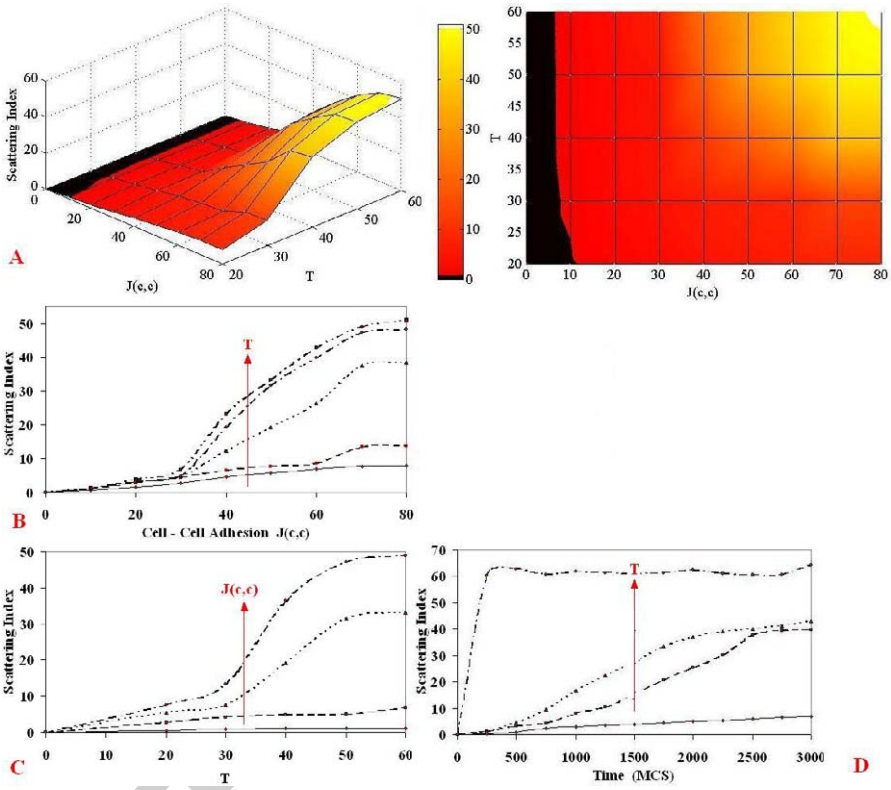

Figure 6: Dissociation process in response of HGF in a culture of ARO cells: Scattering Index at t=3000 MCS, defined as (8), as a function of (A) both cell-cell adhesion energy $J_{c,c}$ and cellular motility T; (B) only of $J_{c,c}$ at $T = 20$ (black solid line), $T = 30$ (black dashed line), $T = 40$ (black dotted line), $T = 50$ (black dash-dotted line) and $T = 60$ (black dot-dot-dashed line); (C) of T at $J_{c,c} = 10$ (black solid line), $J_{c,c} = 30$ (black dashed line), $J_{c,c} = 50$ (black dotted line) and $J_{c,c} = 70$ (black dash-dotted line). (D) Evolution in time of the Scattering Index for $T = 20$ (black solid line), $T = 50$ (black dashed line), $T = 60$ (black dotted line), $T = 80$ (black dash-dotted line). All standard deviations over ten simulations are about 6 per cent of the relative mean values.

they break up in small pieces or fragments, a well-characterized non-biological artifact of the CPM [22], while for the in-range values, the process becomes more significant and quicker for every T-increment.

These results validate our hypothesis that HGF concentration can be modeled increasing simultaneously T and $J(c, c)$, since both an increasing in cell motility and the brokage in E-cadherin bonds are needed for ARO cells scattering, as seen in experimental evidences.

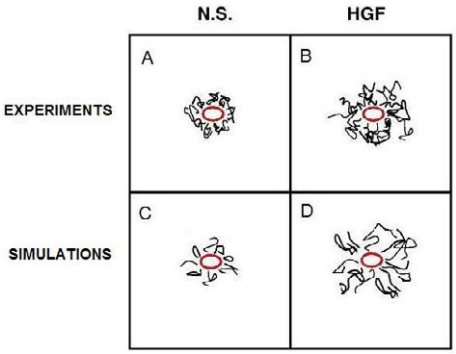

Figure 7: HGF-mediated increase of motility: comparison of single-cell motion tracks obtained by 24-h time-lapse video-recordings (A-B, see [8]) and 3000 MCS simulations (C-D) of ARO cells cultured in the absence (N.S.) and in presence of HGF, as indicated. In the experiments the trajectories are obtained by tracking continuously the motion of the nucleus of a cell, while in the simulations, they are formed by the position of the center of mass of the single cells at each time step. Experimentally, this would correspond to connect the position of the nucleus every 30 seconds (i.e., 1 MCS is set equal to 30 sec). Ten representative tracks were chosen for each case and optimally arrayed for picture presentation. The oval positioned at the center of each group of tracks represent the size of a single cell.

Fig. 7 shows a definitive confirmation of the HGF-induced increase of cell motility, comparing the single-cell trajectories during a 24 h (= 3000 MCS) time-lapse, both in the control and in the stimulated case resulting from the experiment and the numerical simulation: the value of the mean effective distance covered by an ARO cell is about 5 μm in the absence and 12 μm in the presence of the growth factor (means over ten representative cells, error of ≈ 1 μm in both cases).

These evidences are used also to present the basic features of a simulation reproducing a "wound healing" assay, which tests the ability of a cell line to fill gaps created in cell monolayers and is generally considered a simple and reliable test for quantitative evaluation of cell motility. Experimentally, a confluent monolayer of ARO cells, grown in fetal calf serum, is wounded with a pipette tip and incubated for 24 h in the presence HGF, see [8]. In the simulation, Fig. 8, the culture is formed by two masses of 120 virtual cells distributed over an area of about 700 μm $\times$ 700 μm (350 $\times$ 350 lattice sites), while the other parameters are the same as in the simulations of Fig 4. The gap is of about 120 μm (60 lattice sites): the maximum value, deduced from the above results, for which the two colonies encounter within the time limit (24 h). The time needed to invade the space between the colonies is evaluated in Fig. 9 as a function of different cell-cell adhesion parameter values, in the cases of $T = 40$ and $T = 50$. For strong inter-cellular bonds, corresponding to $J_{c,c} < 30$, ARO cells display

barely no detectable healing after 3000 MCS (i.e. nearly 24 hours), which is indicative of an inability to invade the tissue, while for an intermediate range (corresponding to $30 < J_{c,c} < 70$) the time necessary to fill the gap decreases until a sort of limit threshold characteristic of process: about 800 MCS at $T = 40$ and 600 MCS at $T = 50$.

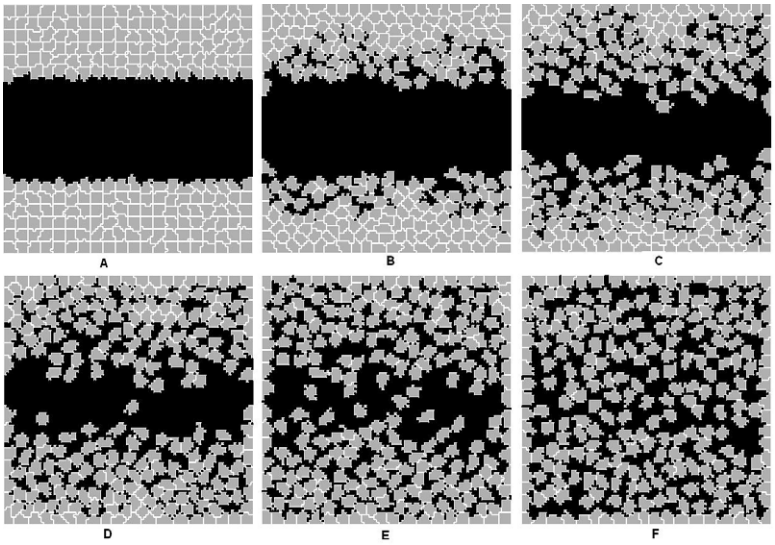

Figure 8: "Wound-healing" process: evolution in time of a simulation initiated with two masses of 120 ARO cells: (A) 1 hour,(B) 8 hours, (C) 12 hours, (D) 16 hours, (E) 20 hours and (F) 24 hours. Full simulation is available at `calvino.polito.it/~preziosi/AROsim2.avi`.

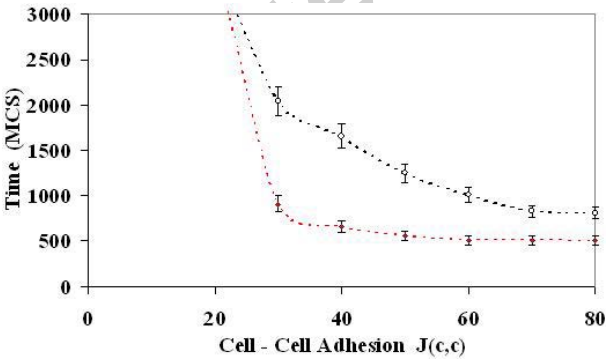

Figure 9: Time for wound healing as function of the cell-cell adhesion energy, for T=40 (red dotted line) and T=50 (black dotted line). Error bars show standard deviations over ten simulations.

Simulation of the Scattering Process of MLP-29 Cells

Figure 10 shows a typical simulation of a time-sequence evolution of a colony of MLP-29 cells in the presence of HGF: we initiate the simulation with a mass of 16 virtual cells, each of them with an area of $\approx 160\ \mu\text{m}^2$ (40 lattice sites), over an area of $\approx 700\ \mu\text{m} \times 700\ \mu\text{m}$ (333×333 sites), which is positioned inside a larger lattice of $1000\ \mu\text{m} \times 1000\ \mu\text{m}$ (500×500 sites) to minimize the boundary effects.

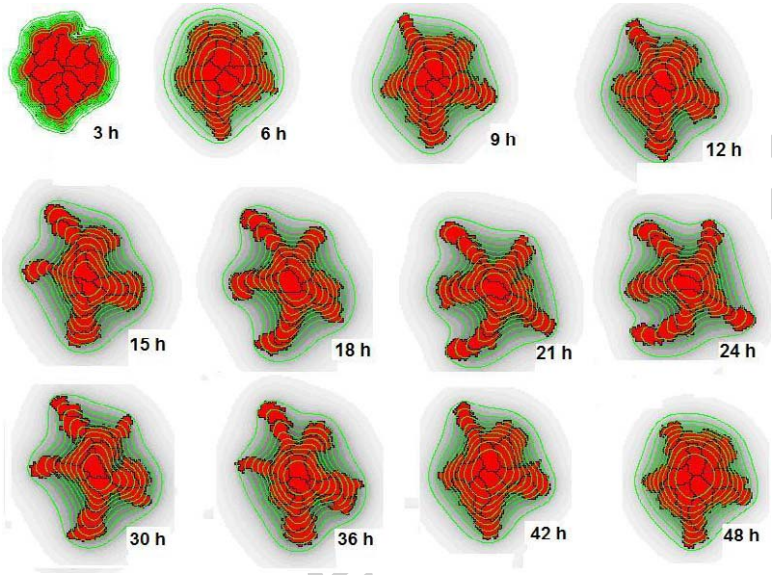

Figure 10: Branching morphogenesis in a simulation initiated with a clump of 16 MLP-29 cells. After 3000 MCS $\approx$ 24 hours the HGF is no longer added in the culture and regression of cell scattering is observed. Isolines (green) indicate ten HGF levels relative to the maximum concentration in the simulation. Full simulation is available at `calvino.polito.it/~preziosi/MLPsim.avi`.

Assuming that the cells do not divide during patterning and in accordance with culture measurements [8], for this sample simulation the HGF's secretion and decay rate are set equal to $10^{-4}\ \text{s}^{-1}$. In this and in the other simulations we set the effective cell-cell adhesion equal to the cell-ECM adhesion (i.e. $J_{c,c} = 2J_{c,M}$, the factor of 2 arise because we model ECM as a single large generalized cell), since experimental analysis suggests a reorganization of intercellular bonds rather than a completely brokage of them. The other parameters are set, in this case, equal to $\lambda = \lambda_{in} = 20$ and $T = 50$.

After an initial stage in which the surface of the colony roughens, with some cells radially protruding from the surface, some branches develop still keeping contact with the neighboring cell and the center of the island: this gives the colony the stellar-shape configuration experimentally found.

As soon as the HGF is no longer added (after 24 hours $\approx$ 3000 MCS), the sprouts start a sort of involution and the island returns compact, a biological behavior that is possible to see also experimentally in [23], see Fig. 10. We model

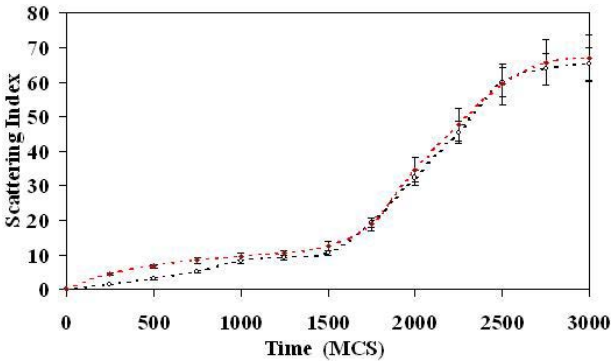

Figure 11: Comparison of the time-evolution of the Scattering Index of a round colony of 16 cells for experimental (red dotted line) and simulation (black dotted line). The parameters of the simulations are those of Fig. 10. Error bar show standard deviations over ten representative islands for the experiments and over ten simulations.

the decay of HGF by imposing $\alpha = 0$ in Eq. (5) (before $\alpha = 10^{-4}$ s^{-1}), while the other parameters are kept unchanged. The evolution of the simulated colony coincides well with the experimental evidences not only qualitatively as shown in Fig. 10, but also quantitatively as it is possible to see in Fig. 11, that compares the time evolution of the Scattering Index of the island as defined in (8) for the experiment and the simulation: it is worth noticing that also the simulated branching develops through the three temporal phases experimentally pointed out in the introduction. The Scattering Index does not significantly increase after $\approx$ 2500 MCS since it is possible to hypothesize an equilibrium between the different forces: the tendency of the cells to elongate and to respond to HGF can no more overcame the adhesion with the rest of the colony and the area constraint. A breakage in this equilibrium would make the scattered island fragment. An analogous behavior is experimentally seen, with the scattered colonies that reach and keep a limit conformation before the detachment of some branches.

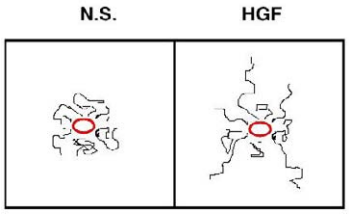

Figure 12: Hepatocyte growth factor-mediated increase of motility as shown by manual time lapse analysis. Single cell motion tracks obtained from 24 hours-lapse simulations of MLP-29 cells culture in the absence (N.S.) and in the presence of HGF. The red oval positioned at the center of the group of tracks represent size of a single cell.

The simulations, confirming the experimental evidences, show a sort of differentiation of the cells in the colonies: those in the sprouts, after the polarization, have a persistence motus in the direction of the branch they belong to, the others (in the valley or in the center) keep a round shape and have a more isotropic

dynamic, see Fig. 12.

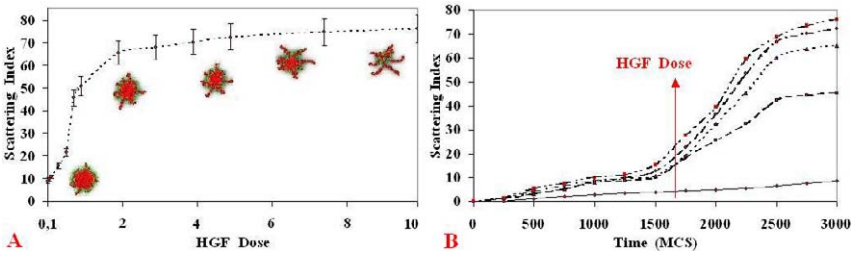

Figure 13: (A) Scattering Index of 16-MLP29 cell clusters after 3000 MCS ($\approx$ 24 h) as a function of HGF secretion rate α. Error bars show standard deviations over ten simulations. Insets are representative configurations after 3000 MCS. (B) Comparison of time evolution of S_I for $\alpha = 10^{-5}$ s^{-1} (black solid line), $\alpha = 10^{-4}$ s^{-1} (black dashed line), $2 \cdot 10^{-4}$ s^{-1} (black dotted line), $5 \cdot 10^{-4}$ s^{-1} (black dot-dashed line) and 10^{-3} s^{-1} (black dot-dot-dashed line). All standard deviations over ten simulations are about 5 per cent of the relative mean values.

To have a deeper idea of the quantity of HGF needed for sprouting and to test whether its dose affects the results, the simulation model is run with increasing values of α ($= \varepsilon$, i.e.), while the other parameters are unchanged. The initial island doesn't sprout for $\alpha < 10^{-4}$ s^{-1}, requiring a minimal level of HGF to start the process, while a sort of phase transition is observed (see Fig. 13) for $\alpha > 10^{-3}$ s^{-1}: between these two values branching process regularly develops.

The tendency of the cells to polarize, elongate, and have a persistent dynamics affects the geometry of the branches. This is studied running a set of simulations keeping the same initial configuration as that in Fig. 10 and gradually increasing λ_{in} (the other parameters are unchanged, with $\alpha = \varepsilon = 10^{-4}$ s^{-1}). For $1 < \lambda_{in} < 45$ the sprouts became longer and thinner with an almost linear trend respect to the λ_{in}-increments. In fact for very low values of the parameter they are almost formed by four or five parallel cells which are not completely polarized, Fig. 14A-B. For $\lambda_{in} > 45$ the branches tend to become only one cell wide and constituted of two or three elongated cells in length. For still higher values, there is a sort of limit threshold: obviously the branches can't be formed by less than a single cell and those which are longer than ≈ 52 μm tend to detach from the main corpus of the colony and, as isolated cells, to migrate in the direction of their longer axes, a behavior also observed in the experiments.

It is also worth noticing that the geometry of the branches is not dramatically influenced by the dose of HGF, since the curves related to different quantities of the growth factor have almost the same slope and don't differ much in the particular values, but may be also related to the number of cells forming the studied island (as shown in Fig. 14C). For this reason some simulations are performed starting with colonies with different densities.

As the number of cells increases, the lattice is taken wider, to avoid overlapping problems. For low densities ($n < 60$) the branches are quite long and thin, so that it can be hypothesized that the colony assumes a stellar-shape configuration, with a little main corpus. For high densities ($n > 60$) the sprouts tend to become shorter and thicker, while at still higher densities ($n > 130$) there are limit thresholds for both length and thickness. The decrement of the

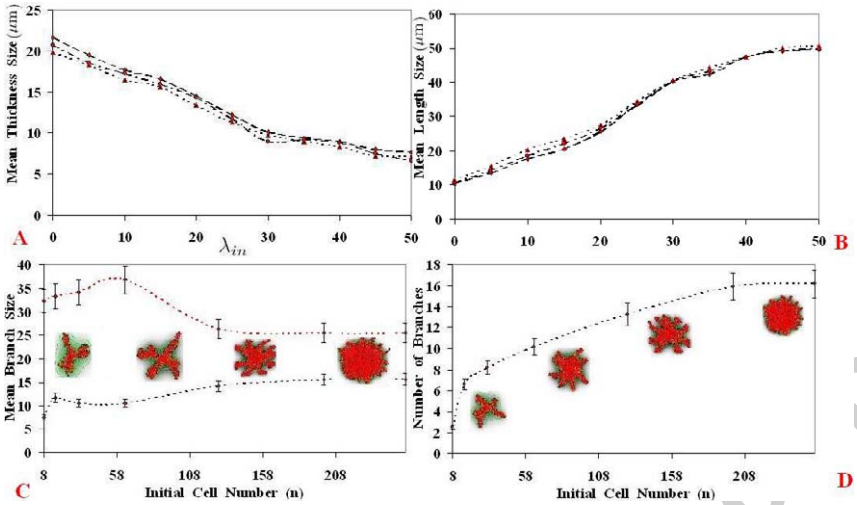

Figure 14: Mean length (A) and mean thickness (B) of the branches formed in a 16 MLP-29 cells round island after 3000 MCS ($\approx$ 24 h) as a function of the persistence penalty coefficient λ_{in} in the cases of $\alpha = \varepsilon = 10^{-4}$ s^{-1} (black dashed lines), $\alpha = \varepsilon = 2 \cdot 10^{-4}$ s^{-1} (black dot-dashed lines) and $\alpha = \varepsilon = 5 \cdot 10^{-4}$ s^{-1} (black dotted lines). All standard deviations over ten simulations are about 4 per cent of the relative mean values. (C) Mean length (red dotted line) and mean thickness (black dotted line) as functions of the initial number of cells forming the colony for $\alpha = \varepsilon = 2 \cdot 10^{-4}$ s^{-1}. (D) Number of the branches formed in a time-lapse of 3000 MCS ($\approx$ 24 h) as a function of the initial cell density of the island. Error bars indicate standard deviations over ten simulations. Insets are representative configurations after 3000 MCS.

length and the relative increment of the thickness is almost specular and has the consequence that the area of a virtual branch remains almost constant, independently from the cell density, which can only lead to a bigger main corpus of the island.

The cell density affects also the number of the branches developing in a time-lapse of 24 h: for very low values ($n < 8$) there is no development of sprouts, for high densities ($n > 108$) there is a constant value for their quantity, as shown in Fig. 14D. In the medium range, the number of the branches increases with the number of cells forming the island. The higher quantity of sprouts appearing in bigger colonies may have two explanations: first, bigger colonies have more cells available for branching, then they have wider external surfaces and so more space for the growth of the sprouts.

In our model we have assumed that the MLP29s' decision to extend or retract a pseudopod depends on the concentration difference between the retracted and extended position of the pseudopods, regardless of the absolute concentration of the HGF. However, at higher concentration we can hypothesize that most HGF receptor will saturate, thus becoming insensitive to HGF levels, a situation that occurs experimentally and that is possible to find also in the sprouting process of blood vessel, [19, 20]

Discussion

We have studied the scattering processes induced by HGF on both ARO and MLP-29 cell lines and shown that the related simulations are in good agreement with experimental results. We have demonstrated that a change in cell-cell adhesion properties, in conjunction with an increment in the system motility, suffices to explain aspects of the biological responses triggered by HGF on a culture of ARO cells. In the absence of HGF the cells are characterized by strong cell-cell junctions, as they form closely adjoined layer, and by a virtual non-motile phenotype: in particular, under normal conditions, ARO cells don't usually detach and move away from the nearest neighbors. On the contrary, HGF induces both the dissociation and invasion programs. This might be related to an interplay with the activity of the cell-adhesion molecule E-cadherin and with its downstream signaling pathways, e.g. via BCL9-2, [2].

In particular, the results of the simulations show that round ARO cells isotropically attract surrounding cells and form rounded, disconnected islands but they haven't acquired autonomous patterning ability (they don't self-organize into polygonal patterns).

The distinctive effects of HGF on ARO cells, i.e., induction or enhancement of motility and invasive growth, are clearly detected at a certain range of doses, since they are not elicited for lower quantities. Therefore it can be concluded that the ARO cells acquire not only an HGF-dependent phenotype but an HGF dose-dependent one.

In the case of a culture of MLP-29 cells, we have shown that the basic model, with a change in cells' adhesive properties and an increased motility, is not sufficient to explain their behavior. It is necessary to add a term related to cell polarization and persistence, in conjunction with a chemotactic response, which were shown to be key ingredients also in the formation of vascular networks [11, 27, 30].

Mimicking contact-inhibition of chemotaxis by suppressing chemotaxis at cell-cell interfaces, our results suggest that the presence of the growth factor produces a continuous, inward, normal force at the cluster boundary, creating a buckling-like instability and that the chemotactic forces compress small initial bumps laterally, producing sprouts. In fact MLP-29 cells are more likely to extend pseudopods than cells in the valley between the bumps.

In other words, cells in growing tips are also more influenced by HGF than those in valleys between tips and in the center of the island: filopodia at growing tips are more frequent because they have a lower energy cost, making the rate of pseudopod extension critical to pattern evolution. For the instability to persist it is required that the cells in the valley must retract, while the others protrude, making the branch they belong to develop.

At equilibrium the tracks of the zones of HGF-action have a quasi-Gaussian profile. It levels off towards the clusters' boundary, while its inflection point is at the cell-cluster boundary.

The simulations suggest that the addition of the growth factor influences the general motility of the culture. The dissociation and the migration of isolated cells permits to study the dynamic of a generic MLP-29. The anisotropic migration requires no extra assumptions in the CPM and produces long persistence time in the presence of HGF cues, because, as seen, cells change direction slowly. The long persistence time introduces two time scales into the branching mor-

phogenesis: the faster along the longer axes produces the growth of the spikes, the slower, radially directed, coarsens the main corpus of the island.

The model has also helped to find the role of the cell shape in the geometry of the branches: the more a cell is elongated and tends to have a persistence dynamics in motion, the more the branch it belongs to is long and thin. Continuum and cell oriented approaches show a correlation between the density of the culture and the equilibrium geometry of the branches: thicker and shorter sprouts form in cell cultures with higher numbers of cells.

In our ongoing work we are refining and validating our computational model by obtaining experimentally derived values for the model parameters and by comparing our simulation results quantitatively to time-lapse videomicroscopy experiments. We also plan to model the interaction of the individual cells with the possibly viscoelastic matrix, which experiments and theory suggest to be crucial in aspects of tissue invasion. An alternative model that can be extended to cover this aspect is presented in [3, 4].

In particular it is possible to discuss how its stiffness and elasticity can explain the relation between the HGF dose and the culture: it is possible to assume that ECM may trap the growth factors to generate a delayed scattering with unstable branches.

From the experimental viewpoint, further experiments are needed to compare morphologies in experiments using different doses of HGF.

Another interesting development is to analyze the dynamics of scattering in other cell lines under different physiological and pathological conditions and compare them to the computational model's dynamics for similar simulated conditions to find a single Hamiltonian which regulates the behavior of different cell lines in response to HGF.

References

[1] Brinkmann, V., Foroutan, H., Sachs, H., Weidner, K. M., Birchmeier, W., 1995. Hepatocyte growth factor/scatter factor induces a variety of tissue specific morphogenic programs in epithelial cells. J. Cell. Biol., 131, 1573 - 1586.

[2] Brembeck, F. H., Schwartz-Romond, T., Bakkers, J., Wilhelm, S., Hammerschmidt, M., Birchmeier, W., 2004. Essential role of BCL9-2 in the switch between beta-catenin's adhesive and transcriptional functions. Genes Dev., 18, 2225 - 2230.

[3] Chauviere, A., Hillen, T., Preziosi, L., 2007. A continuum model for mesenchymal motion in a fibrous network. Networks and Heterogeneous Media. 2, 333 - 357.

[4] Chauviere, A., Hillen, T., Preziosi, L., 2008. Modelling the motion of a cell population in the extracellular matrix. Discr. Cont. Dyn. Sys. B, Supplement Volume, 250 - 259.

[5] Comoglio, P. M., Boccaccio, C., 2000. Scatter factors and invasive growth. Seminar in Cancer Biology. 11, 153 - 165.

[6] Comoglio, P. M., Stella, M. C., 1999. HGF: a multifunctional growth factor controlling cell scattering. Int. J. Biochem. Cell Biol. 31, 1357 - 1362.

[7] D' Alessandro, L., 2006. High-throughput approaches to explore the transcriptional network leading to invasive growth. PhD in: Complex systems applied to post-genomic biology, Torino.

[8] De Luca, A., Arena, N., Sena, L. M., Medico, E., 1999. Met overexpression confers HGF-dependent invasive phenotype to human thyroid carcinoma cells in vitro. J. Cell. Physiol. 180, 365 - 371.

[9] Di Renzo, M. F., Oliviero, M., Narsimhan, R. P., Bretti, S., Giordano, S., Medico, E., Gaglia, P., Zara, P., Comoglio, P. M., 1991. Expression of the Met/HGF receptor in normal and neoplastic human tissues. Oncogene. 6, 1997 - 2003.

[10] Fusco, A., Grieco, M., Santoro, M., Berlingieri, M. T., Pilotti, S., Pierotti, M. A., Dalla Porta, G., Vecchio, G., 1987. A new oncogene in human thyroid papillary carcinomas and their lymph-nodal metastases. Nature. 328, 170 - 172.

[11] Gamba, A., Ambrosi, D., Coniglio, A., de Candia, A., di Talia, S., Giraudo, E., Serini, G., Preziosi, L., Bussolino, F., 2003. Percolation, morphogenesis, and Burgers dynamics in blood vessel formation. Phys. Rev. Letters. 90, 118101.

[12] Glazier, J. A., Balter, A., Merks, R. M. H., Poplawski, N. J., Swat, M.,2007. The Glazier - Graner - Hogeweg Model: Extension, Future Direction, and Opportunitites for Further Study. Single-Cell-Based Models in Biology and Medicine. Chapter II. 4, 157 - 167.

[13] Graner, F., Glazier, J. A., 1992. Simulation of biological cell sorting using a two-dimensional extended Potts model. Phys. Rev. Letters. 69, 2013 - 2017.

[14] Lahat, N., Sheinfeld, M., Sobel, E., Kinarty, A., Kraiem, Z., 1992. Divergent effects of cytokines on human leukocyte antigen-DR antigen expression of neoplastic and non-neoplastic human thyroid cells. Cancer Surv. 69, 1799 - 1807.

[15] Lesko, E., Majka, M., 2008. The biological role of HGF- MET axis in tumor growth and development of metastasis. Frontiers in Bioscience. 13, 1271 - 1280.

[16] Lokker, N. A., Mark, M. R., Luis, E. A., Bennett, G. L., Robbins, K. A., Baker, J. B., Godowski, P. J., 1992. Structure-function analysis of hepatocyte growth factor: Identification of variants that lack mitogenic activity yet retain high affinity receptor binding. EMBO J. 11, 2503 - 2510.

[17] Maere, S., De Bodt, S., Raes, J., Casneuf, T., Van Montagu, M., Kuiper, M., Van de Peer, Y., 2005. Modeling gene and genome duplication in eukaryotes. Proc. Natl. Acad. Sci. USA. 102, 5454 - 5459.

[18] Matsumoto, K., Nakamura, T., 2008. NK4 gene therapy targeting HGF-Met and angiogenesis. Frontiers in Bioscience. 13, 1943 - 1951.

[19] Merks, R. M. H., Glazier, J. A., 2006. Dynamic mechanisms of blood vessel growth. Institute of Physics Publishing. 19, C1 - C10.

[20] Merks, R. M. H., Glazier, J. A., Brodsky, S. V., Goligorksy, M. S., Newman, S. A., 2006. Cell elongation is key to in silico replication of in vitro vasculogenesis and subsequent remodeling. Develop. Biol. 289, 44 - 54.

[21] Merks, R. M. H., Perryn, E. D., Shirinifard, A., Glazier, J. A., 2008. Contact-inhibited chemotactic motility: Role in de novo and sprouting blood vessel growth. PLOS Comp. Biol. 4, e1000163.

[22] Merks, R. M. H., Glazier, J. A., Balter, A., Poplawski, N. J., Swat, M., 2007. The Glazier-Graner-Hogeweg model: extensions, future directions, and opportunities for further study. Mathematics and Biosciences in Interaction. 151 - 167.

[23] Mongiovi, A. M., Huff, J., Jelinek, M. A., Follenzi, A., Gaudino, G., Parsons, J. T., Comoglio, P. M., Medico, E., 1996. The tyrosine kinase receptors Ron and Sea control "scattering" and morphogenesis of liver progenitor cells in vitro. Mol. Biol. Cell. 7, 495 - 504.

[24] Nakamura, T., Teramoto, H., Ichihara, A., 1986. Purification and characterization of a growth factor from rat platelets for mature parenchymal hepatocytes in primary cultures. Proc. Natl. Acad. Sci. USA. 83, 6489 - 6493.

[25] Ramis-Conde, I., Drasdo, D., Anderson, A. R. A., Chaplain, M. A. J., 2008. Modeling the influence of E-cadherin-beta-catenin pathway in cancer cell invasion: a multiscale approach. Biophys. J. 95, 155 - 165.

[26] Sakata, H., Stahl, S. J., Taylor, W. G., Rosenberg, J. M., Sakaguchi, K., Wingfield, P. T., Rubin, J. S. , 1997. Heparin binding and oligomerization of hepatocyte growth factor/scatter factor isoforms. J. Biol. Chem. 272, 9457 - 9463.

[27] Serini, G., Ambrosi, D., Gamba, A., Giraudo, E., Preziosi, L., Bussolino, F., 2003. Modelling the early stages of vascular network assembly. EMBO J. 22, 1771 - 1779,

[28] Stoker, M., Gherardi, E., Perryman, M., Gray, J., 1987. Scatter factor is a fibroblast-derived modulator of epithelial cell mobility. Nature. 21, 239 - 242.

[29] Tamagnone, L., Comoglio, P. M., 1997. Control of invasive growth by hepatocyte growth factor (HGF) and related scatter factors. Cytokine Growth Factor Rev. 8, 129 - 142.

[30] Tosin, A., Ambrosi, D., Preziosi, L., 2006. Mechanics and chemotaxis in the morphogenesis of vascular networks. Bull. Math. Biol. 68, 1819 - 1836.

[31] Trusolino, L., Comoglio, P. M., 2002. Scatter-factor and semaphorin receptors: cell signalling for invasive growth. Nat. Rev. Cancer. 2, 289 - 300.

[32] Weidner, K. M., Behrens, J., Vandekerckhove, J., Birchmeier, W., 1990. Scatter factor: molecular characteristics and effect on the invasiveness of epithelial cells. J. Cell. Biol. 111, 2097 - 2108.

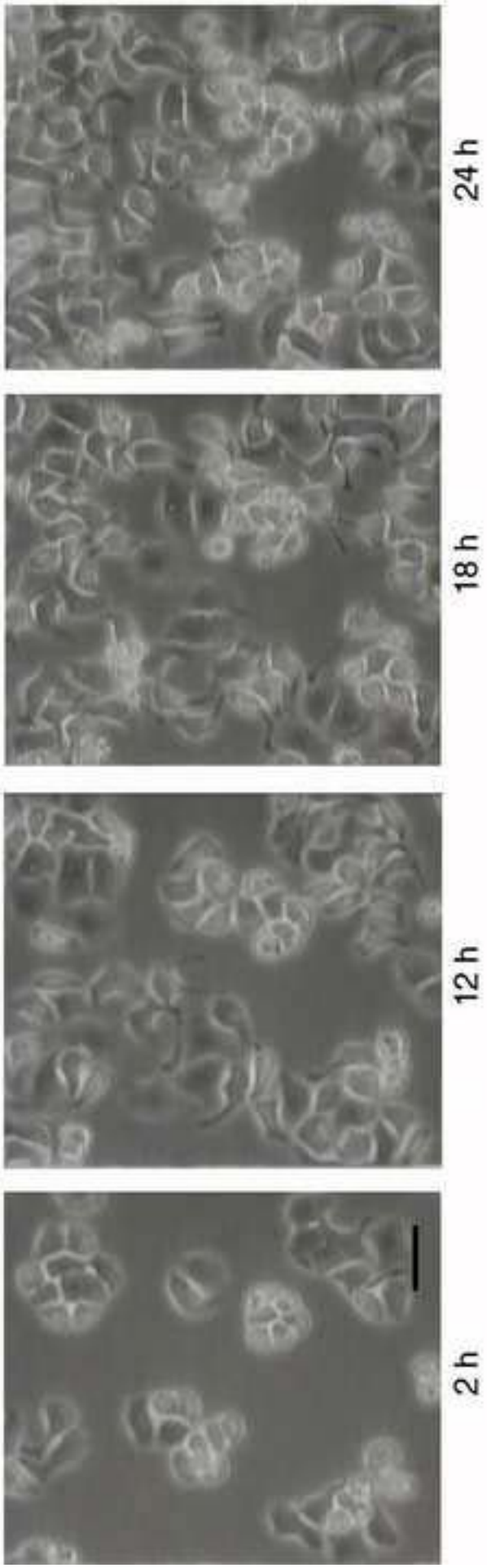

Figure 1

Figure 2

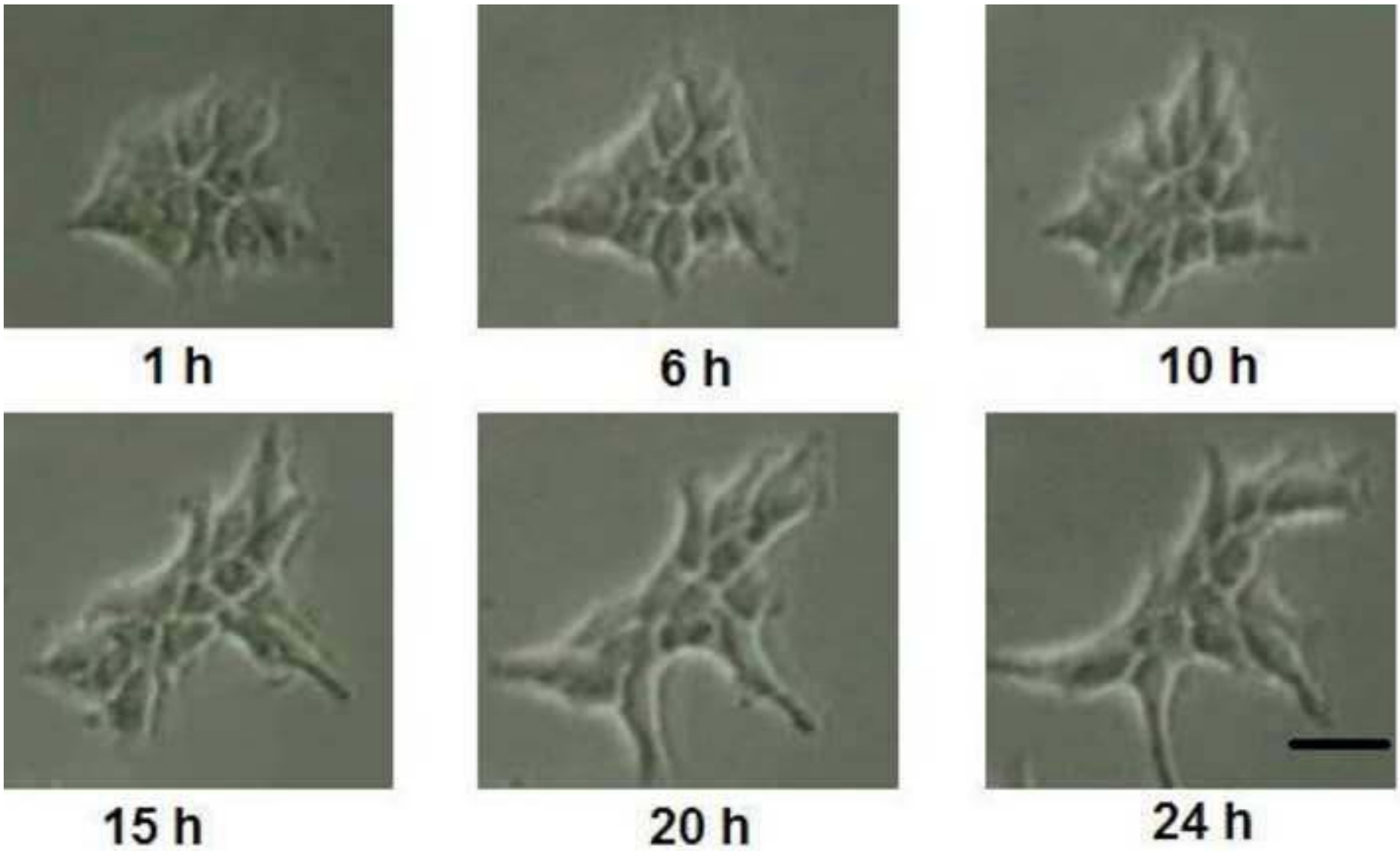

Figure 3

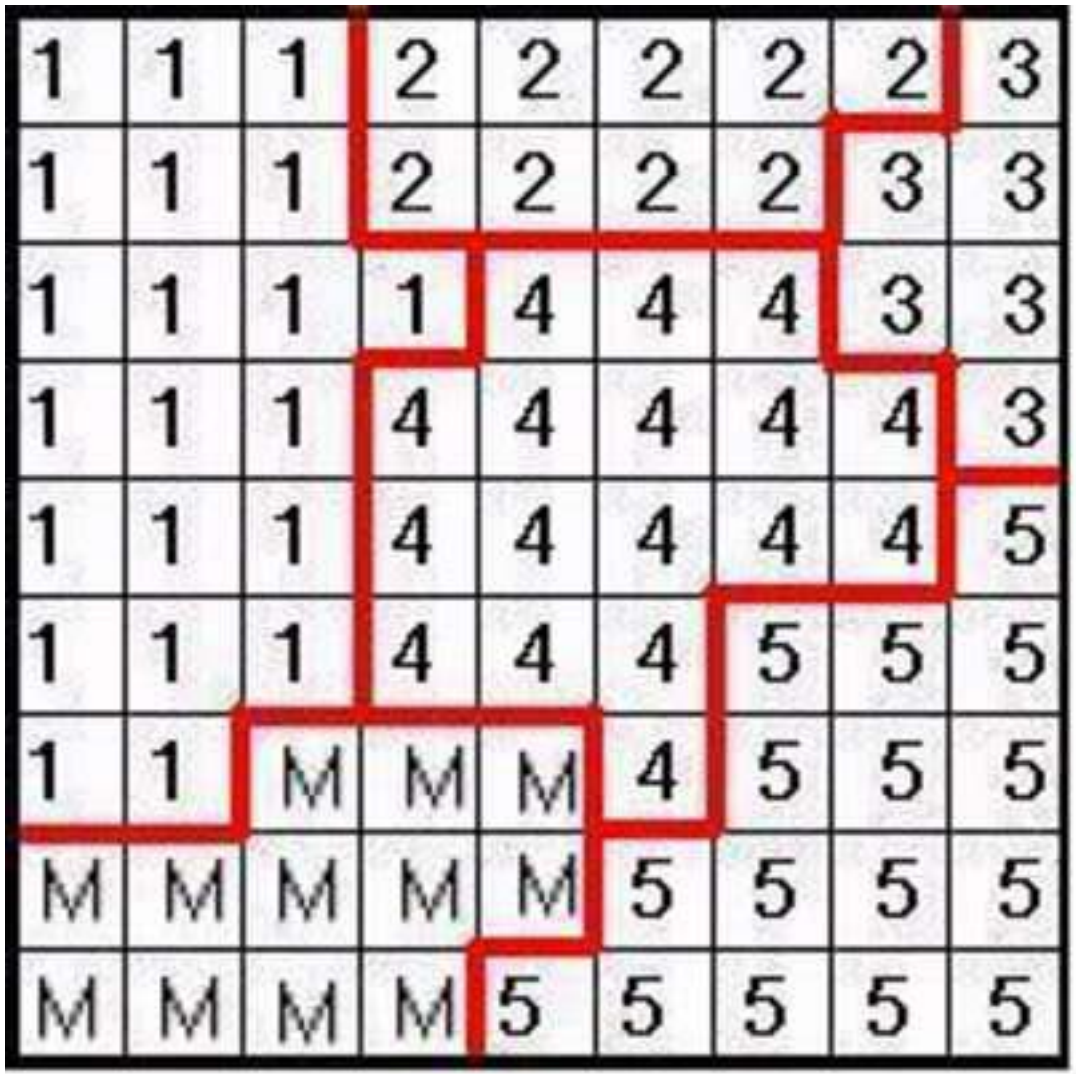

(A)

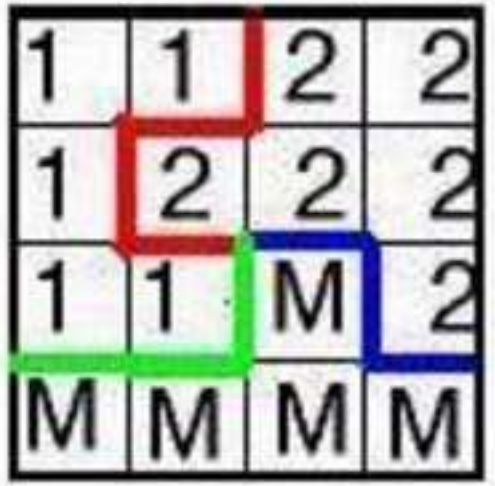

(B)

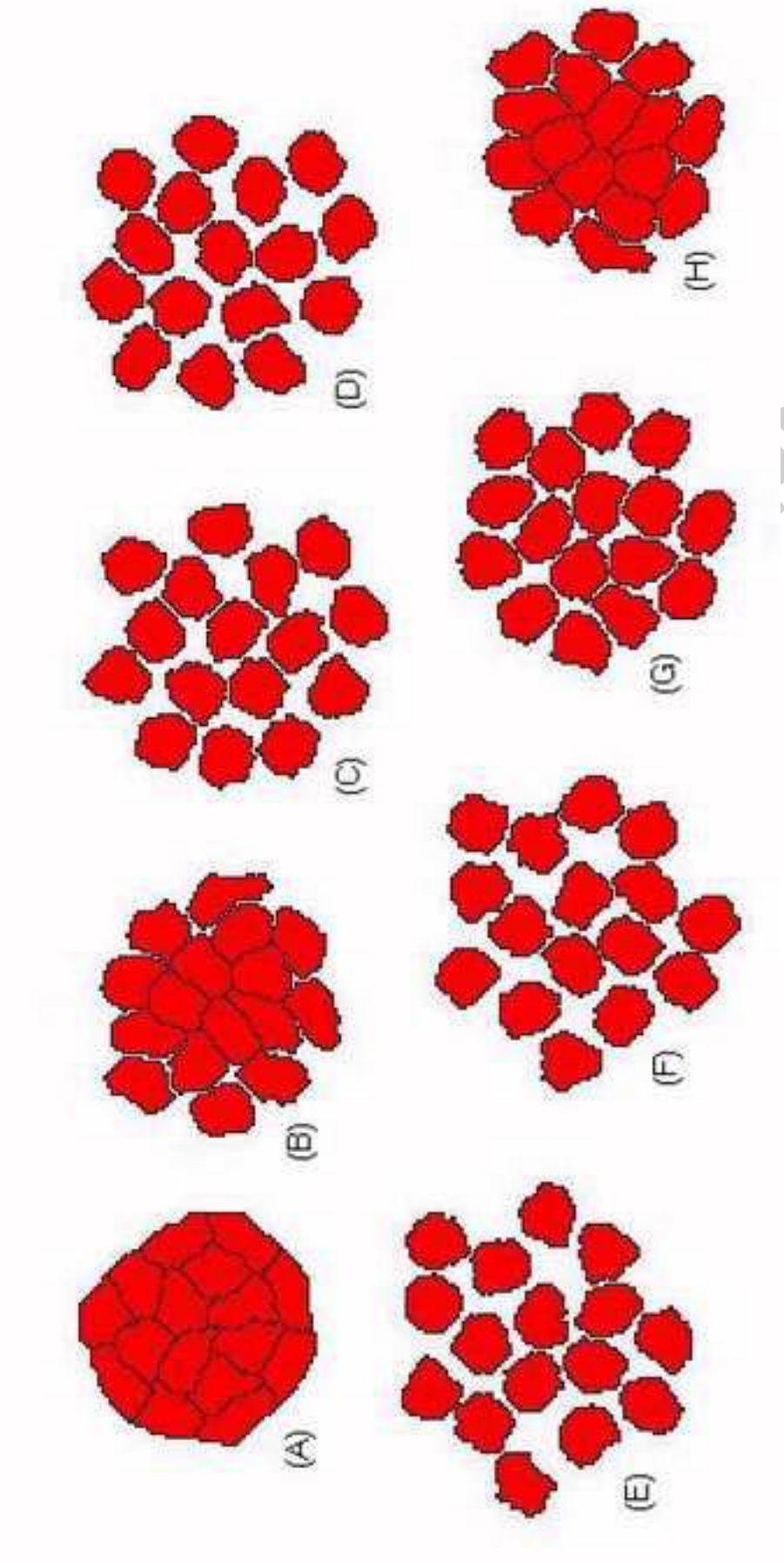

Figure 4

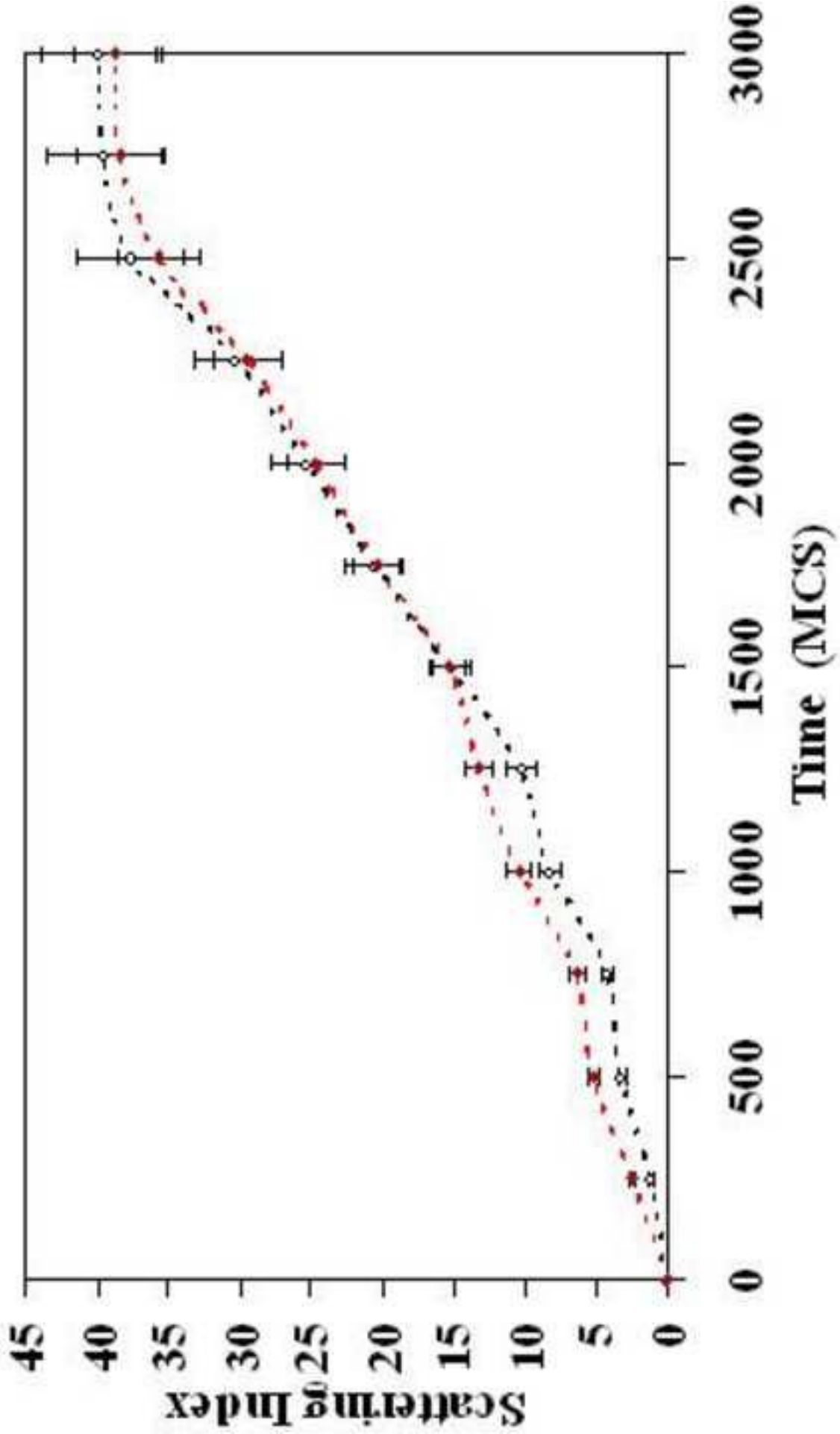
Scattering Index
0
5
10
15
20
25
30
35
40
45
0
500
1000
1500
2000
2500
3000
Time (MCS)

Figure 5

Figure 6

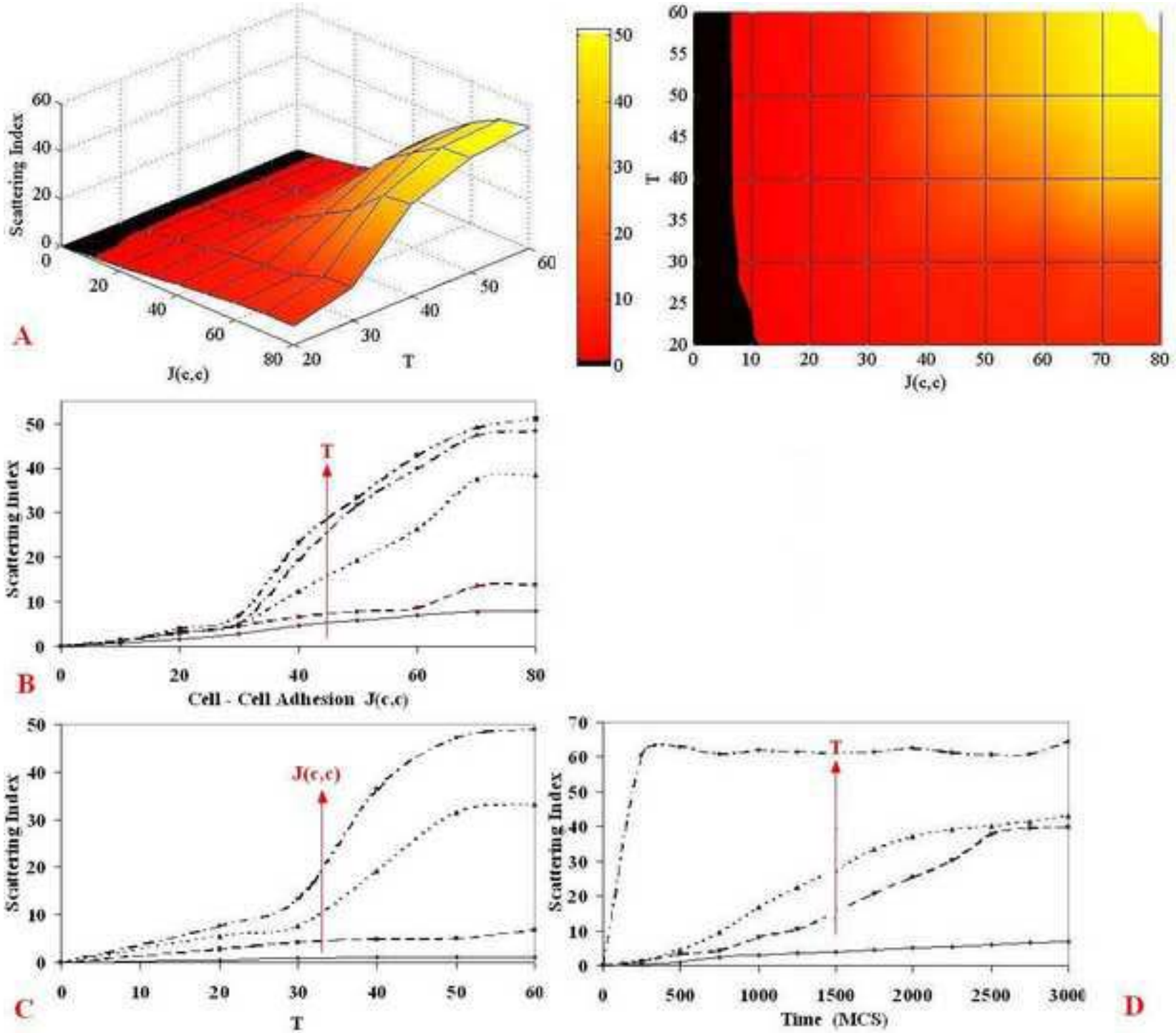

Figure 7

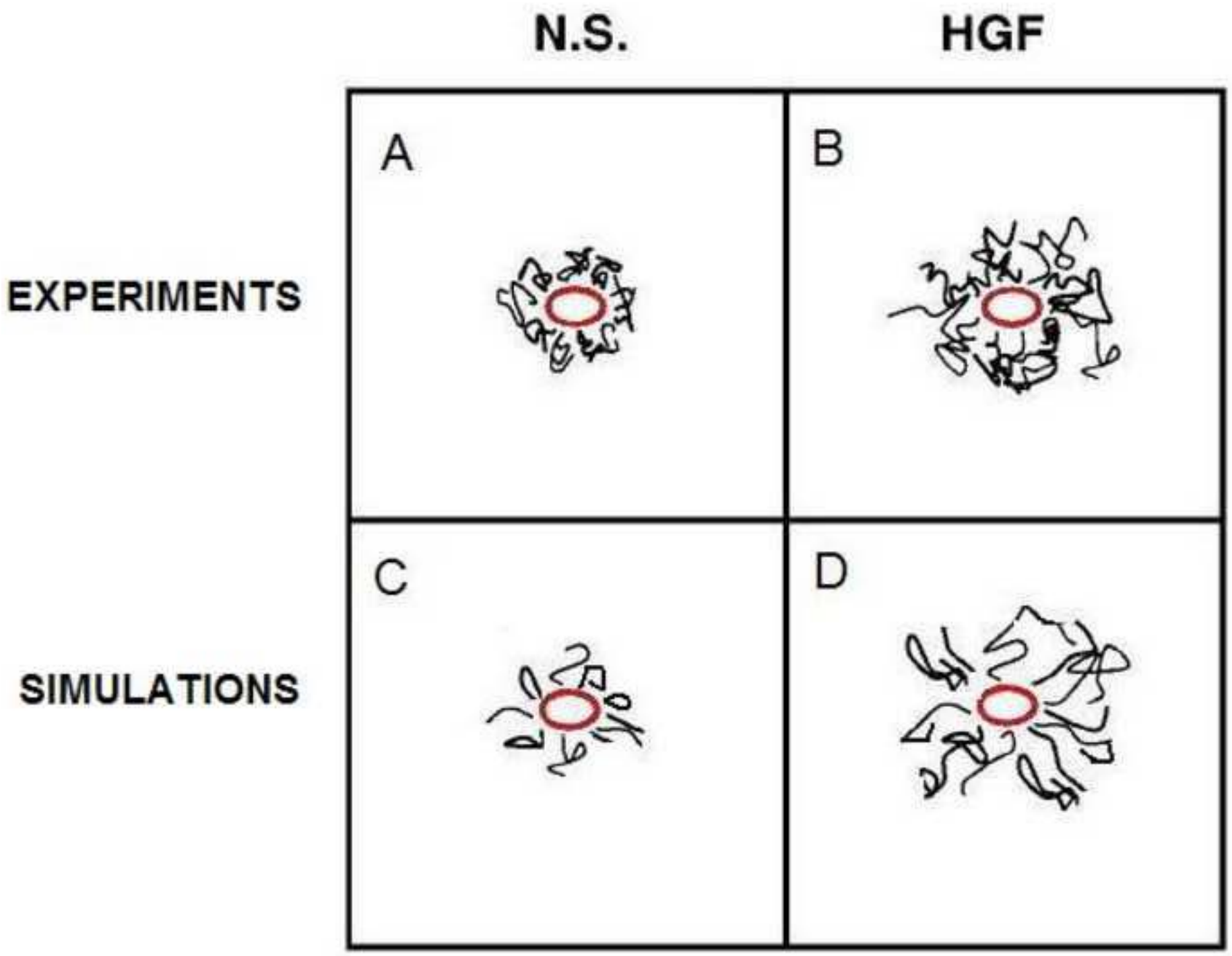

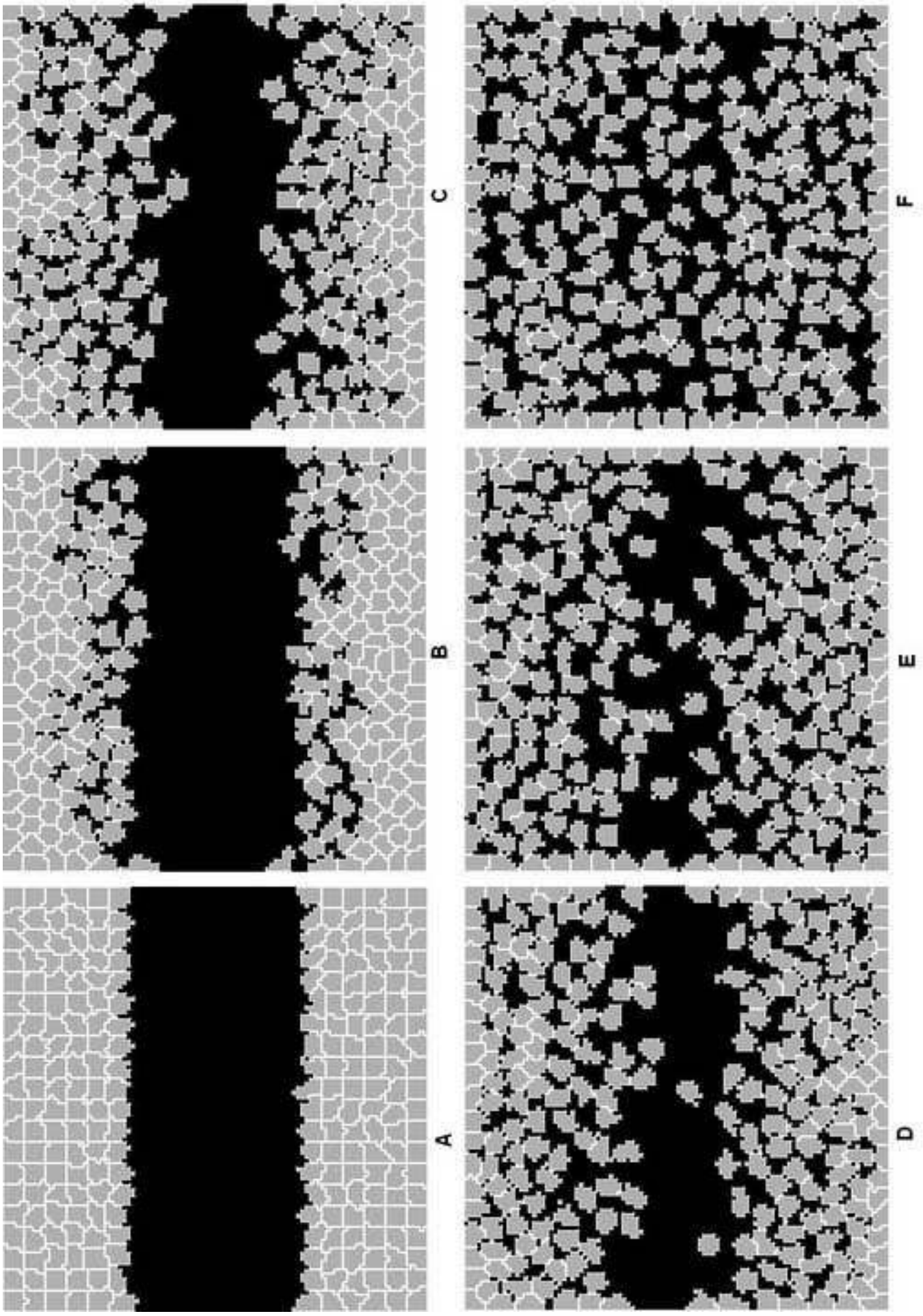

Figure 8

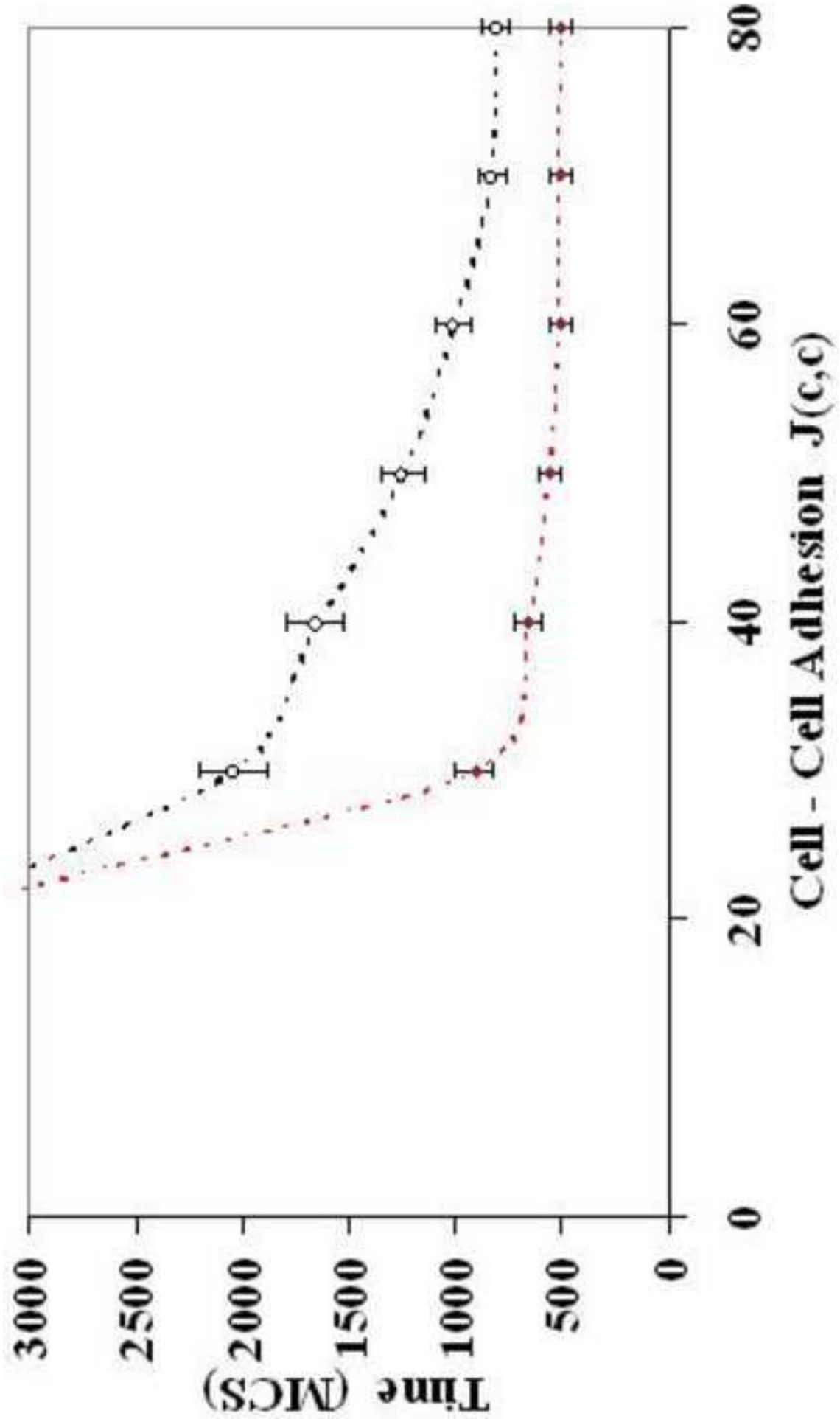

Figure 9

Figure 10

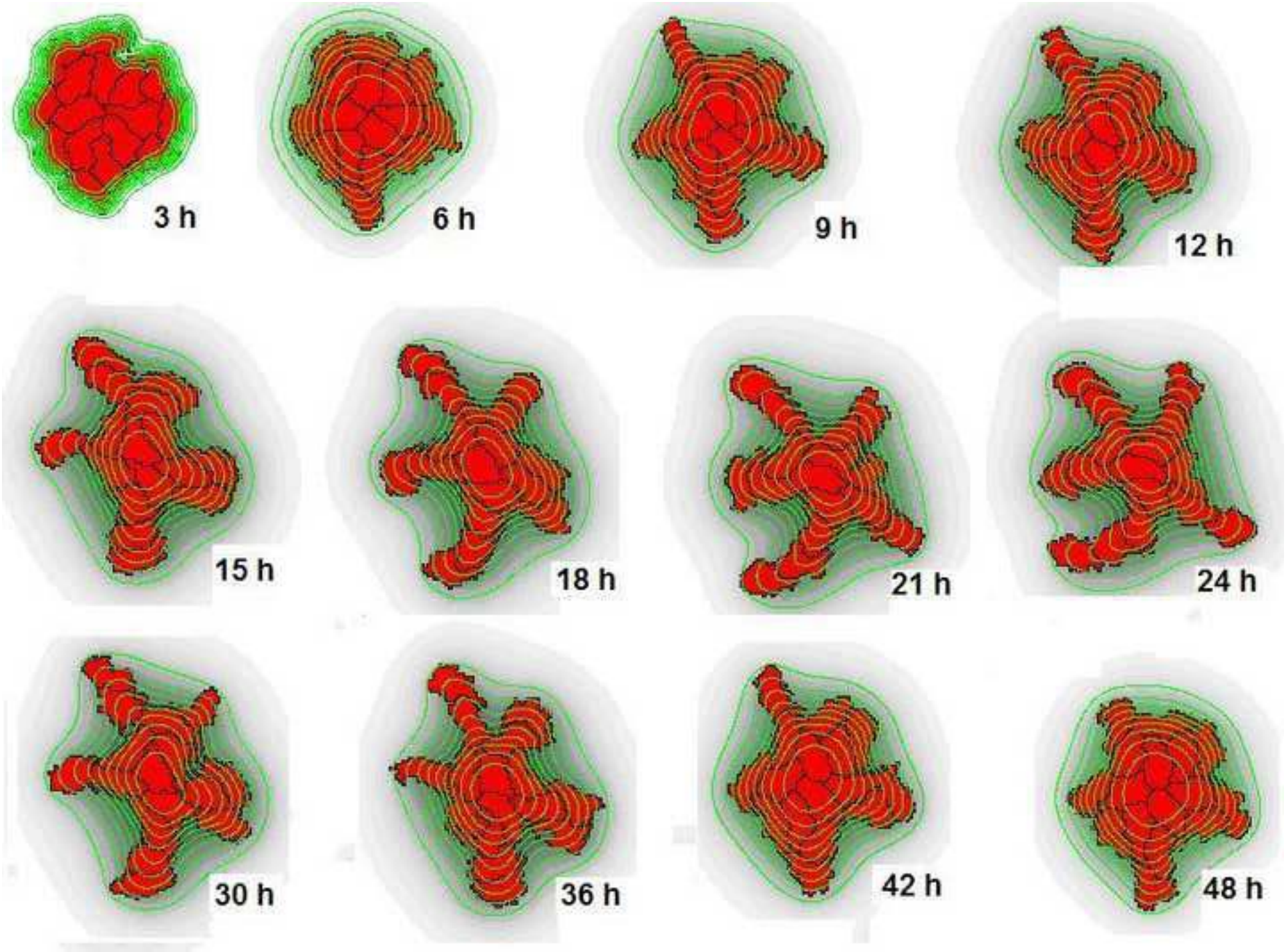

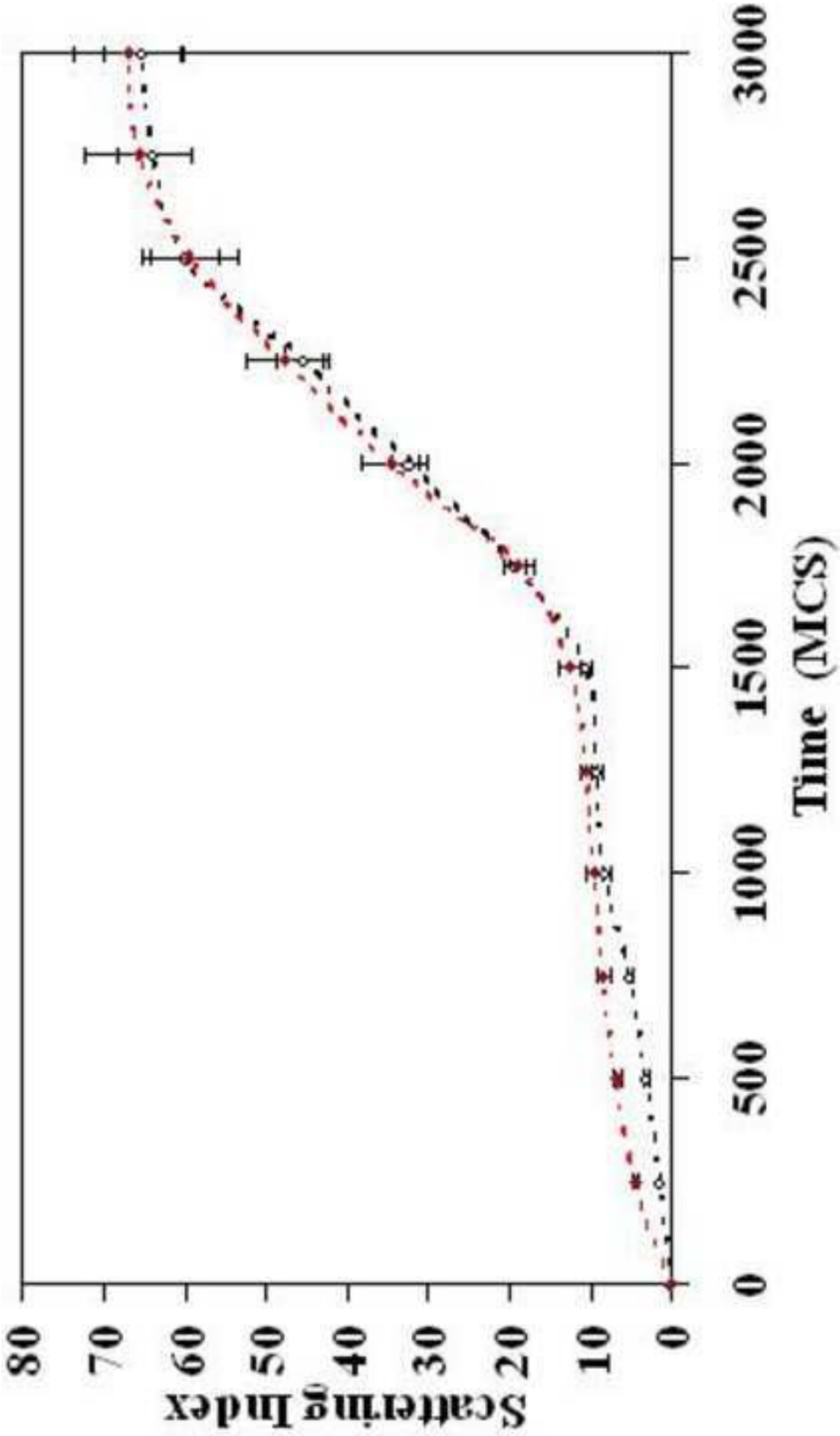
Scattering Index
0
10
20
30
40
50
60
70
80
0
500
1000
1500
2000
2500
3000
Time (MCS)

Figure 11

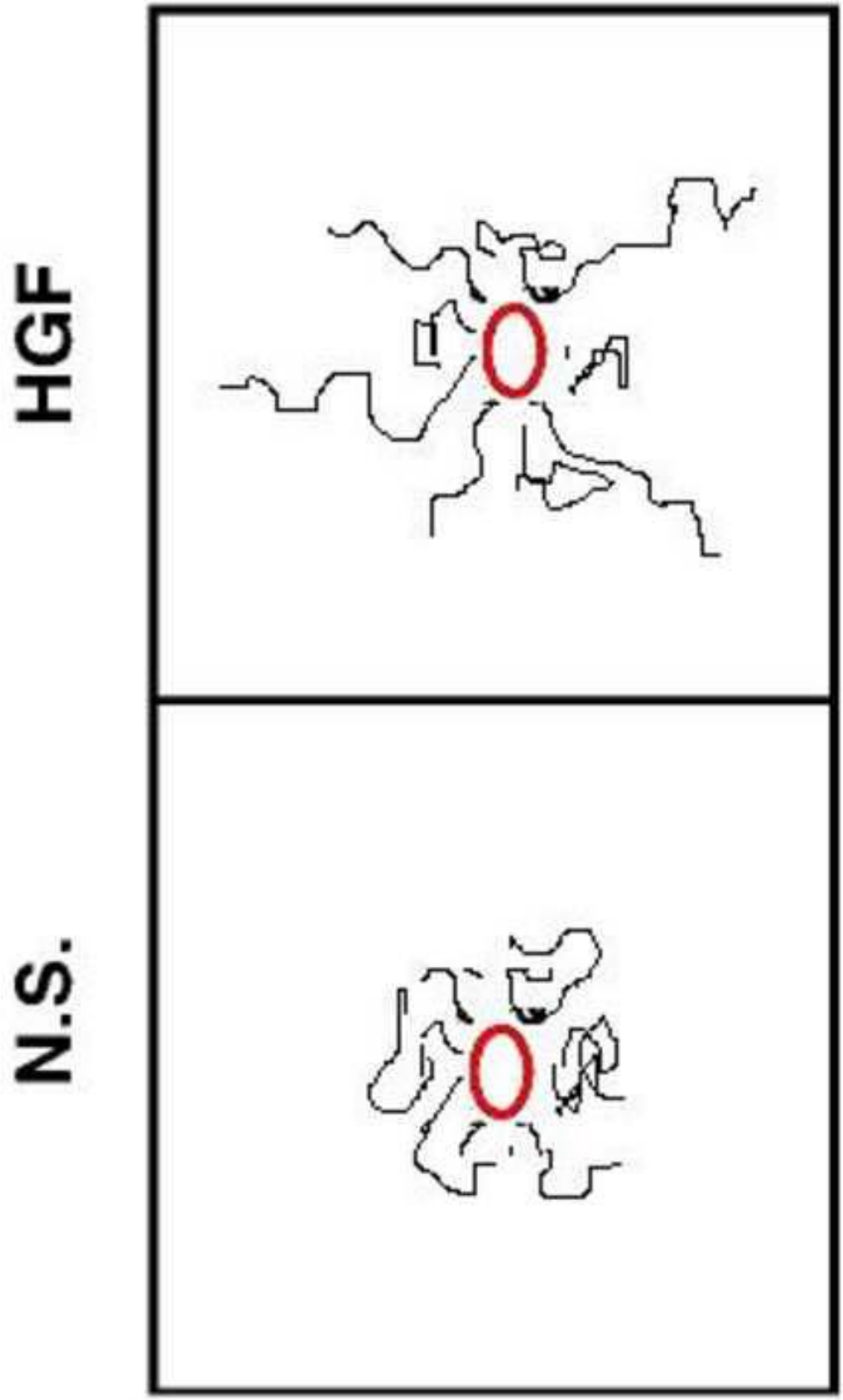

Figure 12

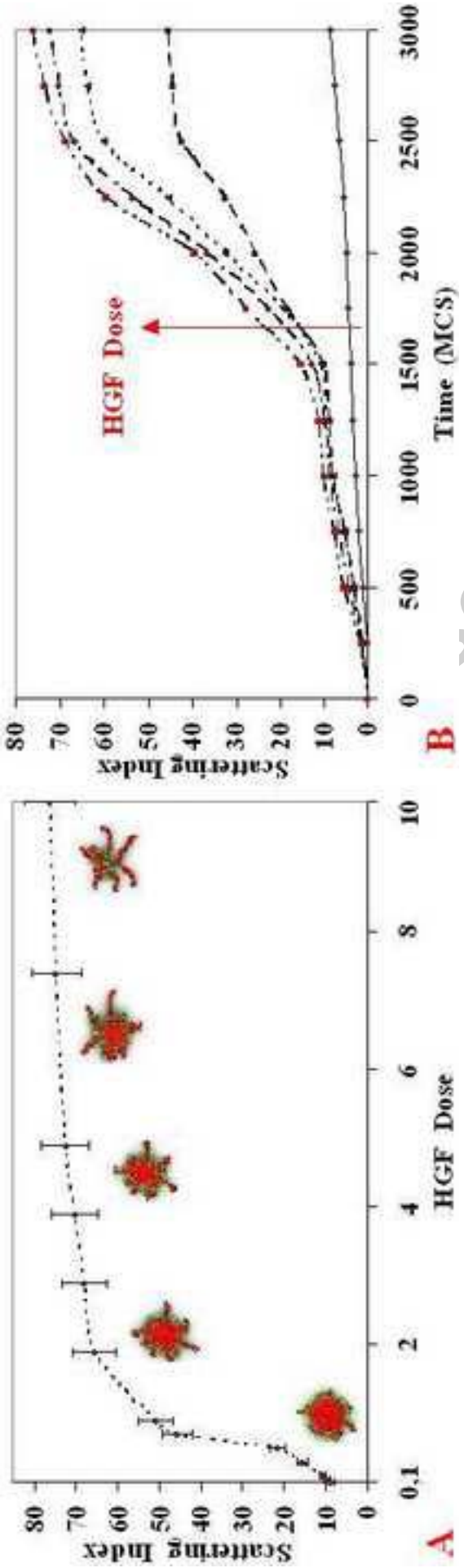

Figure 13

Figure 14

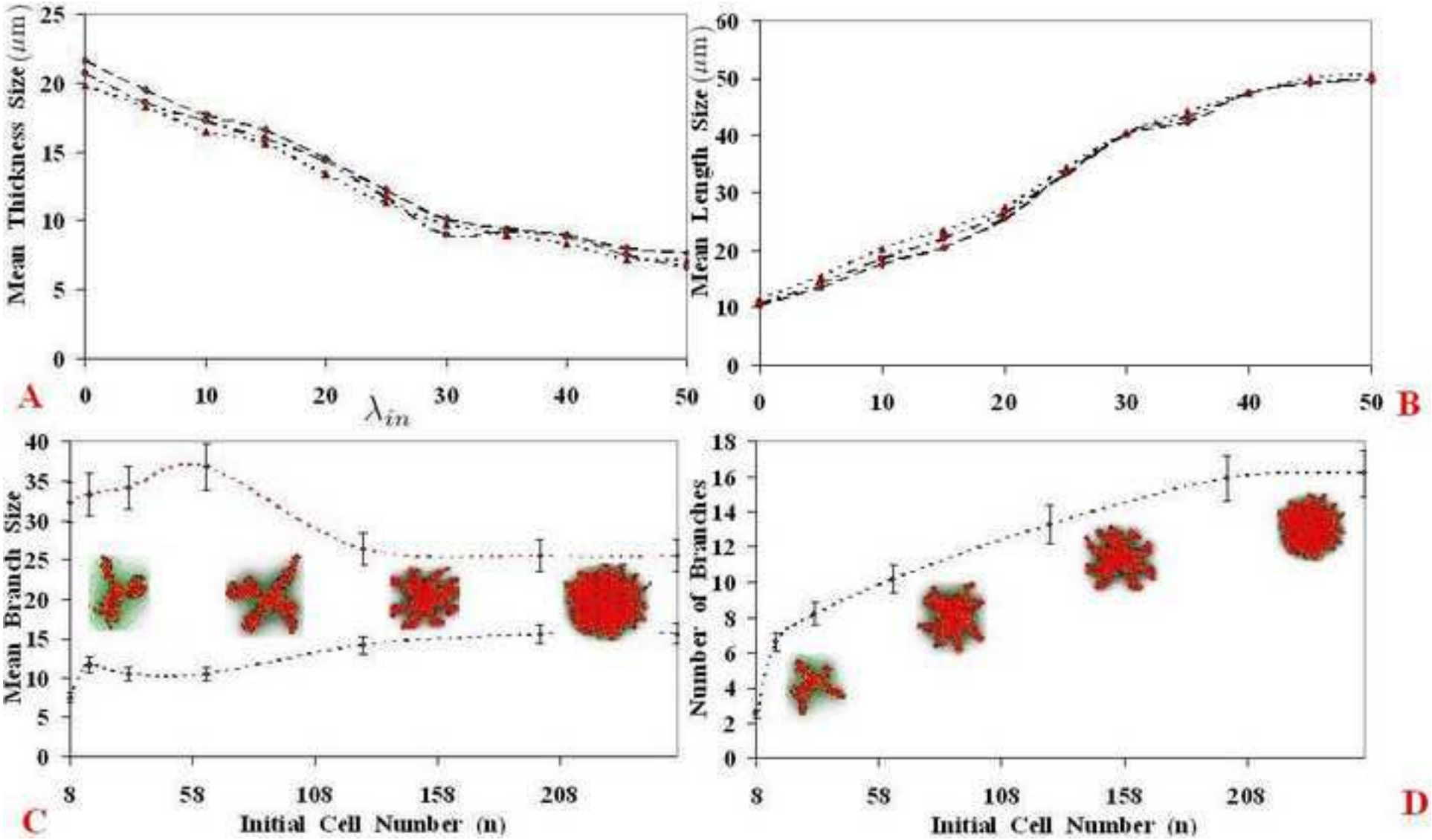

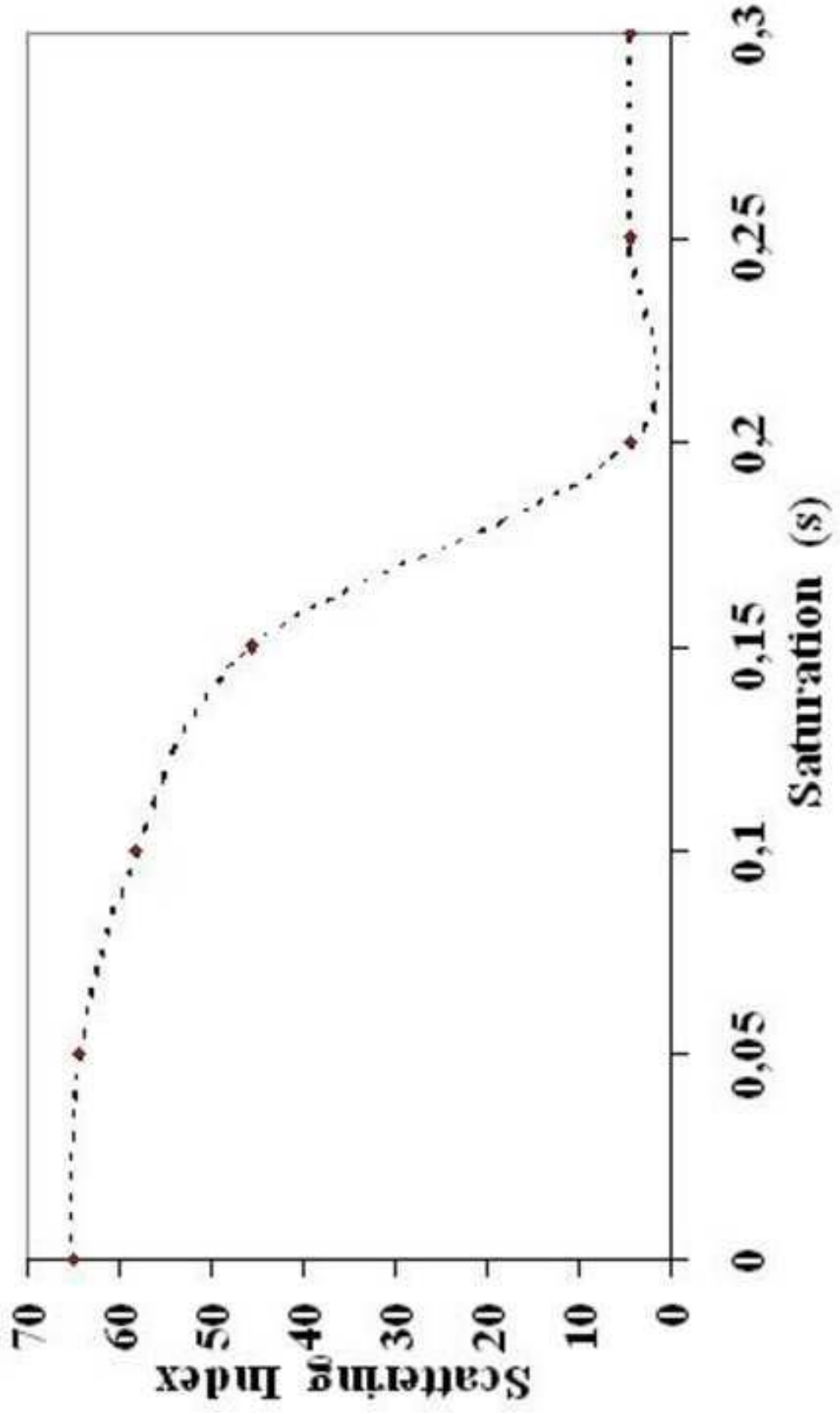

Figure 15